PDF Calculations of Turbulent Nonpremixed Flames with Local Extinction

JUN XU[†] and STEPHEN B. POPE*

Sibley School of Mechanical and Aerospace Engineering, Cornell University, Ithaca, NY

A joint velocity–composition–turbulence frequency probability density function (PDF) model is used to calculate a series of piloted-jet flames of methane. The ingredients of the present model include the simplified Langevin model for velocity, a stochastic model of turbulence frequency, the Euclidean minimum spanning tree (EMST) mixing model, and the 16-species augmented reduced mechanism for methane. The solutions are obtained using a particle/mesh algorithm, and the chemistry mechanism is implemented via the *in situ* adaptive tabulation (ISAT) algorithm. These flames exhibit an increasing amount of local extinction with increasing jet velocity, and are good cases to test the capabilities of turbulent combustion models to account for local extinction in turbulent nonpremixed flames. The calculation results are compared extensively with the experimental data, and demonstrate the ability of the PDF model to represent, quantitatively, the processes of local extinction and reignition that occur in these flames.

INTRODUCTION

Strong effects of turbulent fluctuations on chemical reactions can cause local extinction in nonpremixed turbulent flames when the reactions are slow with respect to the turbulence time scale. Accurate modeling of local extinction phenomena therefore requires a rigorous means of representing such an intense interaction between turbulence and finite-rate chemistry. However, since the interaction between turbulence and chemical reaction is highly nonlinear, it gives rise to the difficulty of tackling this interaction in moment closure models [1], and leads to a number of methodologies: flamelet models [2], probability density function (PDF) methods [3], conditional moment closures [4], and so on. Advances in this research field rely heavily on examining different submodels in the frame of each methodology by comparing their predictions to experimental data.

Numerous experiments have been designed to investigate the structure of nonpremixed flames, and also to provide data sets for testing turbulent combustion models. These include a series of piloted-jet methane flames [5–7] which have been selected as standard test cases [8]. The measurements of piloted-jet methane flames made recently by Barlow and Frank [5] provide a library of comprehensive data which is ideal for testing combustion models. These flames, with different main jet velocities, exhibit different amounts of local extinction, and are accordingly labeled A to F in the order of the increasing jet velocity. Among these flames, flame A is laminar whereas B and C are transitional flames without local extinction. Starting from flame D, local extinction becomes visible, while flame F has significant local extinction. In each of these flames, the amount of local extinction reaches a peak at an axial distance of about 30 jet radii, with reignition occurring further downstream. The severe local extinction in flame F presents substantial challenges to any model, and thus serves as a good validation for the model's description of turbulence–chemistry interactions.

The objective of this study is to apply the most advanced PDF methodology to these flames (namely D, E, and F) to ascertain its ability to calculate the details of local extinction and reignition. The velocity–composition–turbulence frequency joint PDF (JPDF) model [9, 10] has the distinction of taking into account both the chemical reactions and the convection in closed form. Hence, the direct effects of chemical reaction are treated exactly, and the gradient-diffusion assumption is avoided. This model also contains information on the turbulence time scale through modeling the turbulence frequency. The recent progress in mixing models and the efficient implementation of

*Corresponding author. E-mail: pope@mae.cornell.edu

[†]Current address: GE Power System, Combustion Design Engineering, 1 River Rd., Schenectady, NY 12345; E-mail: jun.xu@ps.ge.com

COMBUSTION AND FLAME 123:281–307 (2000)

Published by Elsevier Science Inc.

0010-2180/00/$–see front matter
PII S0010-2180(00)00155-3

TABLE 1

Conditions for Flames D, E, and F

Flame	$U_{j,b}$ (m/s)	$U_{p,b}$ (m/s)	U_c (m/s)	$Re(U_{j,b})$	Features
D	49.6	11.4	0.9	22,400	little local extinction
E	74.4	17.1	0.9	33,600	moderate local extinction
F	99.2	22.8	0.9	44,800	severe local extinction

$U_{j,b}$ = bulk velocity of the fuel jet; $U_{p,b}$ = bulk velocity in the pilot; U_c = free-stream velocity.

detailed reaction mechanisms are also incorporated within the velocity–composition–turbulence frequency JPDF formulation to model Barlow and Frank's flames with the aim of determining the accuracy with which local extinction (and reignition) can be calculated.

The ingredients of the current approach consist ofajointvelocity–composition–turbulencefrequency PDF model; the Euclidean minimum spanning tree (EMST) mixing model [11]; and the augmented reduced mechanism (ARM) of methane oxidation [12] which is computed by the *in situ* adaptive tabulation (ISAT) algorithm [13]. The model equations are solved by the particle/mesh algorithm which is implemented in the code *PDF2DV* [14]. Computational results are compared extensively with the experimental data. These comparisons demonstrate the capability of the current model to calculate accurately and in detail the statistics of these turbulent flames with local extinction.

The background of this study is reviewed in the next section, which is followed by a section describing the PDF and chemical submodels used (i.e., the velocity–composition–turbulence frequency JPDF model, the EMST mixing model, and the ARM for methane). Then, we describe the computational implementation of these models, and the numerics concerned with the calculations. Computational results are presented for mean profiles, conditional mean profiles, conditional PDFs, and scatter plots. The comparisons between the PDF calculations and the experimental data are subsequently discussed, while conclusions are drawn in the final section.

BACKGROUND

Experiments

The piloted-jet flame geometry is proving very useful for the study of turbulence–chemistry interactions since it is fluid-dynamically simple, but still allows strong turbulence effects on the chemistry under conditions approaching extinction. The experimental flows chosen for this study are taken from a series of piloted-jet methane flames (D, E, and F) measured by Barlow and Frank [5].

The experiment setup is now briefly summarized. The fuel jet with radius $R_j = 3.6$ mm is accompanied by an annular pilot ($R_p = 9.2$ mm) which is then surrounded by a slow coflow of air ($U_c = 0.9$ m/s). The jet fuel is a mixture of air and methane in the ratio 3:1 by volume, while the pilot burns a lean premixture of C_2H_2, H_2, air, CO_2, and N_2 with the same nominal enthalpy and equilibrium composition as methane/air at the same equivalence ratio. Such a setup guarantees a low level of hydrocarbon fluorescence interference in the scalar measurements, and reduces the flame length so as to enable high main jet velocity with little or no local extinction [5].

The central jet and pilot velocities are varied (with their ratio being fixed) to yield flames with different extents of local extinction. The conditions for flames D, E, and F are given in Table 1. The measurements in these flames consist of mean scalar profiles, conditional PDFs, and conditional scalar means (both conditioned on mixture fraction) at different locations (x/R_j = 4, 15, 30, 60, 90, etc.) for various species, including H_2O, CO, CO_2, H_2, and OH. However, velocity fields are measured only for flame D by Janicka's research group [15]. These data are available on the Internet from Barlow et al. [16].

The definition of the mixture fraction ξ in the experiments follows the method of Bilger et al. [17], by excluding oxygen from the expression,

$$\xi \equiv \frac{0.5(Y_H - Y_{H,2})/W_H + 2(Y_C - Y_{C,2})/W_C}{0.5(Y_{H,1} - Y_{H,2})/W_H + 2(Y_{C,1} - Y_{C,2})/W_C}, \quad (1)$$

where Y_X denotes the mass fraction of element X in the flame, while $Y_{X,1}$ and $Y_{X,2}$ are the mass fraction of element X in the main jet stream and the coflow stream, respectively. W_X is the atomic weight of element X. From the experimental data, we have $Y_{H,1} = 0.0393$, $Y_{C,1} = 0.117$, and $Y_{H,2} = 0.0007$, $Y_{C,2} = 0.0$. The stoichiometric mixture fraction ξ_s is 0.351 [5].

PDF Calculations of Piloted-Jet Flames

PDF methods at different levels have been used to model piloted-jet nonpremixed flames of methane. Besides the flames of Barlow and Frank, the piloted-jet methane flames of Masri and Bilger [6] have also been widely modeled with PDF methods [18–23]. Generally, these previous calculations used either the IEM (interaction by exchange with the mean) mixing model [24] or the modified Curl's mixing model [25], and used simple chemistry mechanisms (fast chemistry or reduced mechanisms). Saxena and Pope [21, 22], however, adopted in their calculations a skeletal C_1 mechanism of 16 species and 41 reactions (provided by Correa, see also [26]) via the ISAT algorithm, and the joint velocity–composition–turbulence frequency model with the EMST mixing model. Their work shows that the ISAT algorithm is capable of reducing significantly the computational time of implementing detailed mechanisms. However, with the skeletal mechanism, the mass fraction of CO for $\xi > \xi_s$ tends to be overpredicted by as much as a factor of 2. Also, the flame modeled there has almost no local extinction.

Among the flames of Barlow and Frank, flame D is modeled by James et al. [27] using a joint composition PDF method, the k-ϵ model and the skeletal mechanism (the same as that used in [22]) and the ARM mechanisms [12]. In these calculations, the constants in the dissipation model are tuned to yield the mean velocity and mixture fraction profiles that are in good agreement with the experimental data. It is demonstrated that the ARM mechanism is superior to the skeletal mechanism by giving accurate predictions of CO.

Barlow and Frank's D, E, and F flames are also the main target flames of the International Workshops on Measurement and Computation of Turbulent Nonpremixed Flames (TNF) [8, 28]. At TNF4 [28], several researchers reported PDF calculations of these flames, namely Chen (joint composition PDF model, Reynolds stress model, and reduced 12-step mechanism), Hinz et al. (joint composition PDF model, k-ϵ and GRI mechanism with ILDM (Intrinsic Low-Dimensional Manifolds) or reduced 4-step mechanism), and Lindstedt (joint composition PDF model, Reynolds stress model, and reduced 16-step mechanism). The mixing model adopted in these calculations is either IEM or the modified Curl's mixing model. In some cases, it is found necessary to maintain artificially the composition at flamelet values until $x/R_j = 15$ in order to avoid blow-off. Although many of these calculations are quite reasonable for flame D, none captures the essence of the local extinction in flame F (with the possible exception of Lindstedt's calculations). At $x/R_j = 30$ the conditional means are not calculated accurately, and the calculated conditional PDFs do not have the bimodal shape characteristic of local extinction.

The above results provide insights into how to improve the combustion submodels. It is essential to improve the accuracy of chemical mechanisms and the performance of mixing models. One of the principal drawbacks of the IEM mixing model and the modified Curl's mixing model is that they are not local in composition space [11].

In this work, the EMST mixing model is used in conjunction with the ARM mechanism implemented through ISAT to calculate flames D, E, and F of Barlow and Frank. The present model is different from [27] in that the velocity–composition–turbulence frequency JPDF model with the EMST mixing model is adopted; whereas, in contrast to [22], the ARM mechanism instead of the skeletal mechanism is used, and the flames calculated are also different. Moreover, the flames modeled in [22, 27] exhibit little local extinction. The present calculations therefore are to examine extensively the advanced PDF models, in particular their predictability of strong turbulence and finite-rate chemistry interactions.

The description of the EMST mixing model and the ISAT algorithm as well as other submodels and numerical implementations are given in the next two sections.

TABLE 2

Model Constants[a]

C_0	$C_{\omega 1}$	$C_{\omega 2}$	$C_{\omega 3}$	$C_{\omega 4}$	$C_{\omega 5}$	C_Ω	C_ϕ
2.1	0.56	0.9	1.0	0.25	0.2	0.6893	1.5

[a] Note that the effect of C_ϕ is studied by using a range of values, i.e., 1.0, 1.5, 2.0, and 3.0.

JOINT PDF MODEL

The joint velocity–composition–turbulence frequency model provides turbulence time scale information by including the turbulence frequency, and therefore forms a self-contained approach for modeling turbulent flames. Taking the Lagrangian view, which is equivalent to solving the modeled transport equations for the joint PDF by a particle method, the flow is modeled by an ensemble of notional particles. Each particle has its own position $\mathbf{X}^*(t)$, velocity $\mathbf{U}^*(t)$, turbulence frequency $\omega^*(t)$, and compositions $\boldsymbol{\phi}^*(t)$ ($\equiv \{\phi^*_\alpha(t), \alpha = 1, 2, \cdots, \sigma\}$) at time t. Correspondingly, Lagrangian models are established for particle velocities, turbulence frequency, and compositions. These models are described below to make precise the variants of the submodels being used.

Velocity Model

The evolution of particle velocities is modeled by the stochastic differential equation (SDE) of the Langevin type. The general form of the velocity model is written

$$dU_i^* = -\frac{1}{\langle\rho\rangle}\frac{\partial\langle P\rangle}{\partial x_i}\,dt + G_{ij}(U_j^* - \tilde{U}_j)\,dt + (C_0 k\Omega)^{1/2}\,dW_i, \tag{2}$$

where ρ and P are the fluid density and pressure, respectively; "$\langle\ \rangle$" denotes the conventional mean; "$\tilde{}$" represents the density-weighted mean, for example $\tilde{\mathbf{U}} = \langle\rho\mathbf{U}\rangle/\langle\rho\rangle$; the model constant C_0 is given in Table 2; $k \equiv \frac{1}{2}\widetilde{u_i'' u_i''}$ ($u_i'' \equiv U_i - \tilde{U}_i$) is the turbulent kinetic energy; Ω is the conditional turbulence frequency as defined below; while $\mathbf{W}$ is an isotropic Wiener process. The model is completed by providing expressions for the tensor $\mathbf{G}$, which models the effects of pressure fluctuations and viscosity [9, 29, 30]. Here, the simplified Langevin model (SLM) is employed [3], in which $\mathbf{G}$ is

$$G_{ij} = -\left(\frac{3}{4}C_0 + \frac{1}{2}\right)\Omega\delta_{ij}. \tag{3}$$

The SLM model is equivalent to Rotta's model for the pressure-rate-of-strain tensor in Reynolds-stress modeling [29]. It holds a simple form, but gives robust and satisfactory performance in free shear flows.

In terms of the particle velocity $\mathbf{U}^*$, convection is stipulated by the particle movement

$$d\mathbf{X}^*(t) = \mathbf{U}^*(t)\,dt. \tag{4}$$

Turbulence Frequency Model

A stochastic model for the turbulence frequency ω^* of particles was developed [9] to provide a time scale of turbulence. The turbulence frequency is the inverse of the dissipation rate of turbulent kinetic energy k. Alternatively, $\tilde{\omega}$ is analogous to the quantity ω used in the k-ω two-equation model [31]. The stochastic model for ω^* is written [10]

$$d\omega^* = -C_{\omega 3}\Omega(\omega^* - \tilde{\omega})\,dt - S_\omega\Omega\omega^*\,dt + (2C_{\omega 3}C_{\omega 4}\tilde{\omega}\Omega\omega^*)^{1/2}\,dW, \tag{5}$$

where the model constants $C_{\omega 3}$ and $C_{\omega 4}$ are given in Table 2, and S_ω is defined below. In homogeneous turbulence, a gamma distribution is obtained from this model. Moreover, to account for external intermittency effects, the conditional mean turbulence frequency Ω is defined by

$$\Omega \equiv C_\Omega\langle\rho^*\omega^*|\omega^* \geq \tilde{\omega}\rangle/\langle\rho\rangle, \tag{6}$$

where the model constant C_Ω is chosen such that Ω and $\tilde{\omega}$ are equal in fully developed homogeneous turbulence (Table 2). Therefore,

the mean dissipation ϵ is more precisely equal to $k\Omega$, and the turbulence time scale τ becomes

$$\tau \equiv 1/\Omega. \tag{7}$$

In Eq. 5, the source term S_ω is modeled as

$$S_\omega = C_{\omega 2} - C_{\omega 1}\frac{\mathcal{P}}{k\Omega} + C_{\omega 5}\frac{\langle u_j''\rangle}{\langle\rho\rangle k\Omega}\frac{\partial\langle P\rangle}{\partial x_j}, \tag{8}$$

where $\mathcal{P} \equiv -\widetilde{u_i''u_j''}\,(\partial\tilde{U}_i/\partial x_j)$ is the production of k. The values of model constants $C_{\omega 1}$, $C_{\omega 2}$, and $C_{\omega 5}$ are given in Table 2. The choice of $C_{\omega 1} = 0.56$ is discussed in [32]. In addition, variable density effects are considered here which results in the third source term above [33]. Note that in the frame of the current PDF model, the mean of the density-weighted velocity fluctuation $\langle u_j''\rangle$ requires no modeling. For the flames considered here, the term in $C_{\omega 5}$ has but a small effect.

Mixing Model

The conservation equation for the particle's αth composition ϕ_α^* consists of two parts: the micro-mixing process M_α, and the chemical reaction S_α,

$$\frac{d\phi_\alpha^*}{dt} = M_\alpha(t) + S_\alpha(\boldsymbol{\phi}^*(t)). \tag{9}$$

This equation is solved by a time-splitting method in which the mixing term is calculated first, and then compositions are evolved due to the reaction source term. It has been shown that the solution thus obtained is at least of first-order accurate [26].

In PDF models, the micro-mixing process has entailed major modeling efforts. Norris and Pope [34] have shown that the simple IEM model incorrectly predicts local/global extinction in the fast chemistry limit; and that a localized mixing model in composition space is needed to remedy this defect. This mixing localness concept is further explored and demonstrated in [35]. The EMST model developed by Subramaniam and Pope [11] is used in this study. This model performs mixing locally in the composition space through interacting particles with neighboring particles. In other words, in the EMST model, the evolution of the scalar PDF at $\boldsymbol{\phi} = \boldsymbol{\psi}_0$ in composition space is determined solely by the compositions in a small neighborhood of $\boldsymbol{\psi}_0$. As shown in [11, 35], the EMST model can be qualitatively viewed as an extension of mapping closure concepts [36] to multiple scalars.

A full description of the EMST model can be found in [11]. Briefly, as implemented in the present calculations, at any time the model chooses a subset of N_s particles to mix (from the ensemble of N particles in a grid cell) according to the mixing history of each particle which is decided by an age property of the particle. A Euclidean minimum spanning tree is formed in composition space on this subset of N_s particles, so that each particle is associated with at least one neighbor particle. Then, the mixing evolves the compositions of these N_s particles (for $i = 1, \cdots, N_s$) by

$$w^{(i)}\frac{d\phi_\alpha^{(i)}}{dt} = -\gamma\sum_{\nu=1}^{N_s-1} B_\nu\{(\phi_\alpha^{(i)} - \phi_\alpha^{(n_\nu)})\delta_{in_\nu} + (\phi_\alpha^{(i)} - \phi_\alpha^{(m_\nu)})\delta_{im_\nu}\}, \tag{10}$$

where $w^{(i)}$ denotes the numerical particle weight; the νth edge of the tree connects the particle pair (m_ν, n_ν); and δ represents the Kronecker delta. The determination of the model coefficients B_ν and γ is discussed in [11]: in particular γ is obtained through an iterative procedure to achieve the desired decay rate of composition variance due to the mixing. The decay rate is determined by the mixing time scale τ_ϕ which is, according to Spalding [37], modeled by

$$\tau_\phi = \tau/C_\phi, \tag{11}$$

where C_ϕ is an empirical constant.

The quantity of $C_\phi = \tau/\tau_\phi$ is the velocity-to-scalar timescale ratio, which in shear flows is found to range from 1.5 to 2.5 [38]. The more recent inert round-jet measurements of Panchapakesan and Lumley [39] yield $C_\phi = 1.5$. In the present work, the influence of C_ϕ is examined by performing calculations with different values of C_ϕ between 1.0 and 3.0. It is found that the calculation of local extinction (in particular in flame F) is sensitive to the specified value of C_ϕ, and the best agreement with the experiments is obtained using $C_\phi = 1.5$. Hence

we take $C_\phi = 1.5$ as the base-case value, rather than the traditional value of $C_\phi = 2.0$ originally proposed by Spalding [37]. Of the eight model constants given in Table 2, C_ϕ is the only one that is adjusted by reference to the Barlow and Frank's data. Many results are also reported using the conventional value $C_\phi = 2.0$.

The performance of the EMST mixing model has previously been tested in a periodic reaction zone [40] and by the previous PDF calculations of piloted-jet flames [22] of Masri and Bilger [6]. However, it is yet to be challenged by more complex flames, especially those with significant local extinction (e.g., flame F).

Chemistry Mechanism

An accurate chemistry mechanism is necessary to describe a flame accompanying strong turbulence–chemistry interaction. In contrast, the skeletal mechanism used in [22] is shown to give poor results (for $\xi > \xi_s$) since it does not contain C_2 species [27]. Hence, a detailed mechanism (e.g., the GRI mechanism) is desired to be implemented with PDF methods. However, such a mechanism usually involves tens to hundreds of species, and PDF methods require an efficient means to implement such a mechanism so as to be computationally tractable. Therefore, various reduced mechanisms (typically involving four reactions) are widely used. However, it is recognized that some of the crucial intermediate species may not exist in steady state over an extensive thermodynamic parameter range as assumed normally in these reduced mechanisms. The relaxation of these assumptions can lead to a reduced mechanism that contains a moderate number of species and reactions, but yields significant improvement in modeling complex combustion systems with strong turbulence–chemistry interactions.

Sung et al. [12] recently derived an ARM from GRI-mech 1.2 for methane oxidation through relaxing the quasi-steady-state (QSS) assumptions for some C_2 species. This mechanism consists of 16 species and 12 reaction steps, and has been tested at various circumstances, such as perfectly stirred reactors, laminar flames, and counterflow nonpremixed flames with extinction and ignition [12]. The ARM has also been shown to give better performance than the skeletal mechanism in the joint composition PDF calculation of flame D [27]. We use ARM in the current calculations implemented using the ISAT algorithm [13].

NUMERICAL SOLUTION PROCEDURE

In this section, we describe the numerical and computational methods used to solve the joint PDF transport equation, including the implementation of chemical reaction.

Particle/Mesh Method

As discussed in the previous section, the fluid is represented by a set of particles whose properties evolve according to the Lagrangian models (Eqs. 2, 4, 5, and 9). The computational domain is decomposed into small cells to represent and to estimate mean fields (such as the mean velocities $\tilde{U}_i$). Such a particle/mesh method has been implemented in the *PDF2DV* code which solves the modeled velocity–composition–frequency joint PDF equation for statistically stationary two-dimensional (plane or axisymmetric) turbulent flows, in particular reacting flows [14]. This code uses a rectangular mesh. The flames considered here are statistically axisymmetric, so the computational domain is a rectangle in the x-r plane, and the equations are solved in the form appropriate to the axisymmetric geometry.

The *PDF2DV* code uses a pseudo-time marching scheme to solve the SDEs in many small time steps Δt. Statistics of the solution evolve from the specified initial condition until the statistically stationary state of interest is reached. The time step Δt is chosen to ensure that both the Courant number (based on particle velocities and the local mesh spacing) and $\Omega\Delta t$ are small compared to unity. Typically, the maximum values of the Courant number and $\Omega\Delta t$ are 0.6 and 0.5, respectively. At any time t, the mean fields are required to advance the particle equations. In *PDF2DV*, the mean fields are represented as linear splines based on the nodal values, which are estimated by a cloud-in-cell method [41]. Once the statistically stationary state is reached, the solution is continued for some time so that mean quantities can be

time-averaged to reduce the statistical error [10].

To enforce the mean continuity equation and to obtain the mean pressure field, correction algorithms are devised for particle position and velocities. At first, the position correction is performed to satisfy the consistency condition, which states that the volume associated with a subensemble of particles equals the geometric volume occupied by the particles. Then, the particle velocities are corrected so that the divergence of the mean mass flux vanishes. As a result of the correction, mean pressure is obtained as well. These algorithms are described in detail in [42].

Finally, *PDF2DV* is parallelized using a particle partitioning approach [43]. In this study, the parallel computation is also implemented for the EMST model to improve the computational efficiency as well as to retain the numerical accuracy of EMST [44].

The overall numerical features of this particle/mesh algorithm for the JPDF model may be found in [10]. In brief, the scheme is (by numerical experiments with the piloted-jet flame of Masri et al. [6]) demonstrated to be convergent in terms of the number of particles in each cell (N_{pc}) and the cell size. The statistical error converges at the rate of $N_{pc}^{-1/2}$; the bias is proportional to N_{pc}^{-1}; and the spatial discretization error is second-order with respect to the cell width. The statistical error is further reduced by time-averaging. The choice of the numerical parameters and the resulting numerical accuracy of the calculations are discussed in "Numerical Parameters."

ISAT: Implementation of Chemical Reaction

Computational intractability and the lack of an efficient algorithm have been limiting the application of detailed chemistry mechanisms in combustion modeling. Even the implementation of the ARM mechanism includes 16 species and 12 reaction steps, and requires a fast algorithm. In this study, this task is accomplished by the ISAT algorithm developed by Pope [13].

The ISAT algorithm is in essence a storage/retrieval technique for the calculation of composition changes due to chemical reaction. The fundamental quantity stored and retrieved is the reaction mapping $\mathbf{R}(\boldsymbol{\phi}^0)$, which is defined to be the solution to the reaction equation

$$\frac{d\boldsymbol{\phi}}{dt} = \mathbf{S}[\boldsymbol{\phi}(t)], \tag{12}$$

over the time step Δt from the initial condition $\boldsymbol{\phi}^0$. This is exactly the quantity needed in the solution of the particle composition equation (Eq. 9) using the method of fractional steps [26].

An essential observation is that realized compositions of reaction are restricted to a small subset of the composition space—the accessed region. In contrast to the direct integration (DI) of the reaction equation, or *a priori* table storing the reaction mapping in the whole composition space, the ISAT algorithm builds adaptively an unstructured table of the reaction mapping only for the accessed region. The table is built in the course of the PDF computation, and an *in situ* data retrieval or DI is conducted according to a prescribed error tolerance ϵ_{tol}.

A table entry in the ISAT algorithm consists of: the initial composition vector $\boldsymbol{\phi}^0$; the mapping $\mathbf{R}(\boldsymbol{\phi}^0)$; the mapping gradient $\mathbf{A}(\boldsymbol{\phi}^0)$; and the specification of the ellipsoid of accuracy (EOA, a hyper-ellipsoidal region centered at $\boldsymbol{\phi}^0$). For any query $\boldsymbol{\phi}^q$, the linear approximation to the mapping is

$$\mathbf{R}(\boldsymbol{\phi}^q) \simeq \mathbf{R}(\boldsymbol{\phi}^0) + \mathbf{A}(\boldsymbol{\phi}^0)(\boldsymbol{\phi}^q - \boldsymbol{\phi}^0). \tag{13}$$

By definition, the EOA is the region around $\boldsymbol{\phi}^0$ in which the normalized error in this approximation is less than ϵ_{tol}. If $\boldsymbol{\phi}^q$ lies within the EOA at $\boldsymbol{\phi}^0$, then $\mathbf{R}(\boldsymbol{\phi}^q)$ is retrieved using the linear approximation. Otherwise, DI is performed to obtain $\mathbf{R}(\boldsymbol{\phi}^q)$, and also the error between this new mapping and the approximate mapping is measured. If the error is smaller than ϵ_{tol}, the EOA is grown and $\mathbf{R}(\boldsymbol{\phi}^q)$ is returned; otherwise, a new record is generated based on $\boldsymbol{\phi}^q$.

The details and the tests of ISAT algorithm are described in [13, 22]. It has also been applied to turbulent nonpremixed flames in [22, 27]. It is shown that ISAT can speed up the computation of chemical reaction by as much as a factor of 1000 in comparison with the full direct integration of the mechanism. For piloted-jet nonpremixed flames, the speed-up factor

is typically 40 to 100 [22, 27]. In this study, the generated table in one PDF calculation is often used in subsequent calculations to enhance further the computational speed. The accuracy of ISAT is determined by the error tolerance ϵ_{tol}. The appropriate value of ϵ_{tol} depends on the accuracy required, the chemical mechanism, the time step Δt, and the accessed region. In the previous calculations of piloted-jet flames using ISAT [22, 27], ϵ_{tol} is assigned values from 8×10^{-3} to 8×10^{-4}. In this work, $\epsilon_{tol} = 5 \times 10^{-5}$ is used. The accuracy achieved using this error tolerance with the ARM mechanism is determined using the PMSR (Pairwise Mixing Stirred Reactor) test case [13] with the inflow stream compositions of the piloted-jet flame computations. The results of these tests (reported in [44] and [45]) show that with the error tolerance used ($\epsilon_{tol} = 5 \times 10^{-5}$) the error in mean species mass fraction is less than 1%.

Computational Domain and Boundary Conditions

For the piloted-jet flame calculations, we use a cylindrical coordinate system with the origin at the center of the fuel jet. The computational domain covers a rectangular area of $(0, 25R_j)$ in radial direction and of $(0, 120R_j)$ in axial direction. In the computations, velocity and length are normalized by the centerline velocity at the inlet U_j and the jet radius R_j, respectively.

In a PDF calculation, the initial and boundary conditions are defined for the joint PDF, and specifically defined for particles. At the inlet, the velocity PDF is prescribed to be joint normal, and the appropriate gamma distribution is assigned to turbulence frequency. Both of them have the prescribed means derived as follows. The mean axial velocity $\tilde{U}$ and the Reynolds normal stress $\widetilde{u''u''}$are inferred from experimental data [16]. The mean radial velocity $\tilde{V}$ is taken to be zero, and the remaining normal stresses $\widetilde{v''v''}$ and $\widetilde{w''w''}$ are each taken to be equal to $\widetilde{u''u''}/2$. However, there are no data on the covariance $\widetilde{u''v''}$ nor on mean frequency $\tilde{\omega}$. As pointed out in [10], the boundary conditions at the inlet for these two quantities are crucial for the turbulence frequency model. Here, the mean turbulence frequency and $\widetilde{u''v''}$ are specified in the same manner as [10]. Figure 1 presents these inlet boundary conditions. Inlet boundary conditions for compositions and temperature are deduced from experimental data [16] and are shown in Table 3. Note that, based on the experimental data, the pilot temperature in flames D, E and F are taken to be 1880 K,

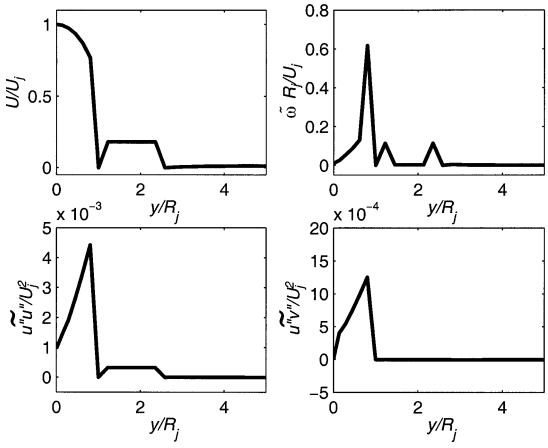

Fig. 1. Inlet profiles of mean quantities for flame D.

TABLE 3

Specifications of Boundary Conditions for Compositions (Specific Mole Numbers, Y_α/W_α) in Different Streams at the Inlet[a]

Streams	Pilot	Coflow	Jet
T	1880.0	291.0	294.0
P	0.993	0.993	0.993
H_2	6.4026×10^{-5}	0.0	0.0
H	2.5010×10^{-5}	0.0	0.0
O_2	1.6997×10^{-3}	7.3718×10^{-3}	6.1407×10^{-3}
OH	1.6507×10^{-4}	0.0	0.0
H_2O	5.2311×10^{-3}	3.4773×10^{-4}	0.0
HO_2	0.0	0.0	0.0
H_2O_2	0.0	0.0	0.0
CH_3	0.0	0.0	0.0
CH_4	0.0	0.0	9.7472×10^{-3}
CO	1.4506×10^{-4}	0.0	0.0
CO_2	2.4960×10^{-3}	0.0	0.0
CH_2O	0.0	0.0	0.0
C_2H_2	0.0	0.0	0.0
C_2H_4	0.0	0.0	0.0
C_2H_6	0.0	0.0	0.0
N_2	2.6220×10^{-2}	2.7053×10^{-2}	2.3101×10^{-2}

[a] Note that these conditions are the same for flames D, E, and F except that in the flame F, the temperature of the pilot stream is 20° K lower according to the experimental data.

1880 K, and 1860 K, respectively. Boundary conditions other than the inlet condition, include outflow conditions at the outlet boundary ($x = 120R_j$), reflecting (axisymmetric) conditions at the centerline ($y = 0$) and free stream boundaries ($y = 25R_j$). These conditions are imposed straightforwardly at the particle level. Finally, the particles are initialized to possess the same conditions as the inlet boundary; but the statistically stationary state does not depend on the details of the initial conditions.

Numerical Parameters

Numerical parameters in the computation include the number of cells in the domain (or grid size), the number of particles per cell N_{pc}, and the time step. The numerical behavior with respect to these parameters has been studied by the present authors [10], and the accuracy of the EMST mixing model with respect to N_{pc} is examined in [46]. The numerical parameters below are thus chosen following these studies.

A nonuniform rectangular 61×61 grid is used with a finer spacing near the centerline and the inlet. The nominal number of particles in each cell N_{pc} is approximately 100, which is the same as that used in the previous PDF/ISAT/EMST calculation of piloted-jet flames [22]. A constant time step $\Delta t = 0.3R_j/U_j$ is used, which satisfies the restrictions described in "Particle/Mesh Method." For the three flames D, E, and F this yields $\Delta t = 1.7112 \times 10^{-5}$ s, 1.1408×10^{-5} s, and 8.556×10^{-6} s, respectively.

The choice of these numerical parameters is partly due to the constraints of available computer resources. Some calculations are performed on an Intel cluster (Pentium II 450 MHz) and others on an IBM SP2 supercomputer. In both cases, five processors are used to perform a single calculation. It takes about 100 to 120 hours per processor (i.e., 500 to 600 processor hours) for a job starting from scratch to reach a statistically stationary solution in about 3000 time steps. About 90% of the total CPU time is spent on the ARM/ISAT calculations of chemical reaction. By the end of calculation, about 19,000 records are generated in the ISAT table.

The numerical accuracy achieved using the above parameters has been comprehensively evaluated [44, 45]. It is shown [44, 45] that numerical errors in mean and r.m.s. profiles are around 10% for $x/R_j \leq 30$, less than 20% at $x/R_j = 60$, but larger at $x/R_j \geq 90$ and for Reynolds stresses. Statistics conditioned on mixture fraction display considerably less numerical error. Clearly, gains in computational efficiency are desirable so that more accurate calculations (e.g., $N_{pc} = 400$ on a 100×100 grid) can be performed at reasonable cost. Nevertheless, the accuracy of the present calculations is sufficient to test the model's ability to predict local extinction and reignition, which occur at $x/R_j \leq 60$.

RESULTS

In this section, PDF calculations are compared to the experimental data of Barlow and Frank's flames D, E, and F. As described in "Joint PDF Model," the JPDF model consists of SLM, the variable density model of turbulence frequency, EMST, and ARM (implemented via ISAT). The model constants used are given in Table 2. The mixing model constant C_ϕ is varied to investigate its influence on the calculation of turbulence–chemistry interactions. The base case calculations are performed with $C_\phi = 1.5$.

As discussed above, the numerical error in the calculated mean and root mean square (rms) profiles may be unacceptably large for $x/R_j \geq 90$. Consequently, in general, results are presented only up to $x/R_j = 60$; and the axial profiles beyond this point are not considered to be reliable.

Profiles of Means and Variances

Since the velocity data are available only for flame D, the PDF calculations are first compared to the experimental data for this flame. The calculated statistics are weighted by mass. Figures 2 and 3 show radial profiles of the mean and variance of velocity and mixture fraction plotted against the experimental data at three axial locations. The direct effect of increasing C_ϕ from 1.5 to 2.0 is to increase the mixing, and hence to decrease $\widetilde{\xi''^2}$. This affects the mean density, and thereby the mean and rms velocity. In general, the agreement between the calcula-

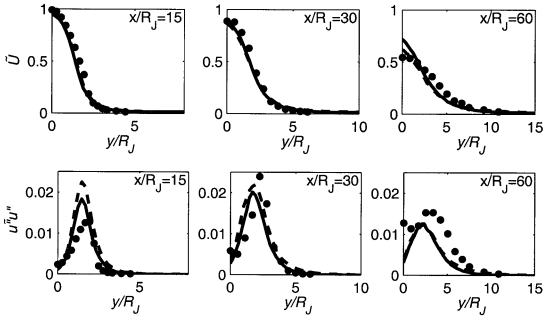

Fig. 2. Radial profiles of flame D. Symbols, experiment; lines: PDF calculations with $C_\phi = 2.0$ (solid) and $C_\phi = 1.5$ (dashed).

tions and the experimental data is reasonable, the largest discrepancies being for the variances at $x/R_j = 15$.

The comparison between the calculated radial profiles of the means and variances of other scalars and the experimental data is presented in Figs. 3–6 for flames D and F.

The profiles of the rms of mixture fraction, ξ'', show how the mixing is affected by different

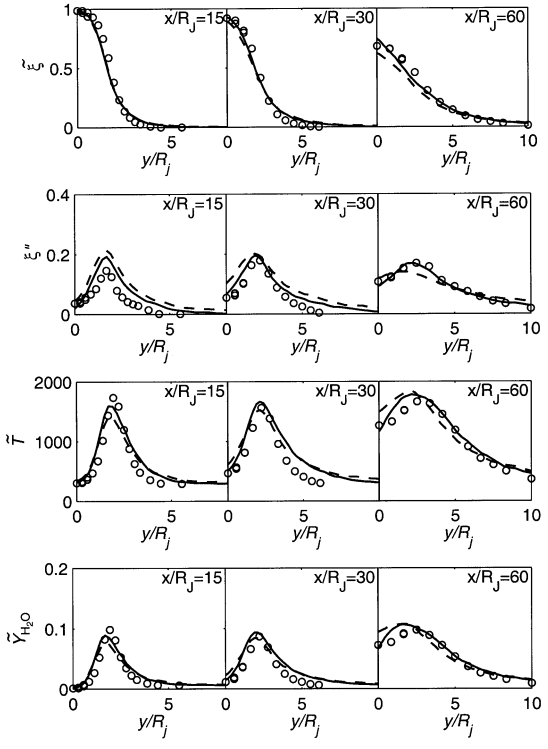

Fig. 3. Radial profiles of flame D (continued). Symbols, experiment; lines: PDF calculations with $C_\phi = 2.0$ (solid), $C_\phi = 1.5$ (dashed).

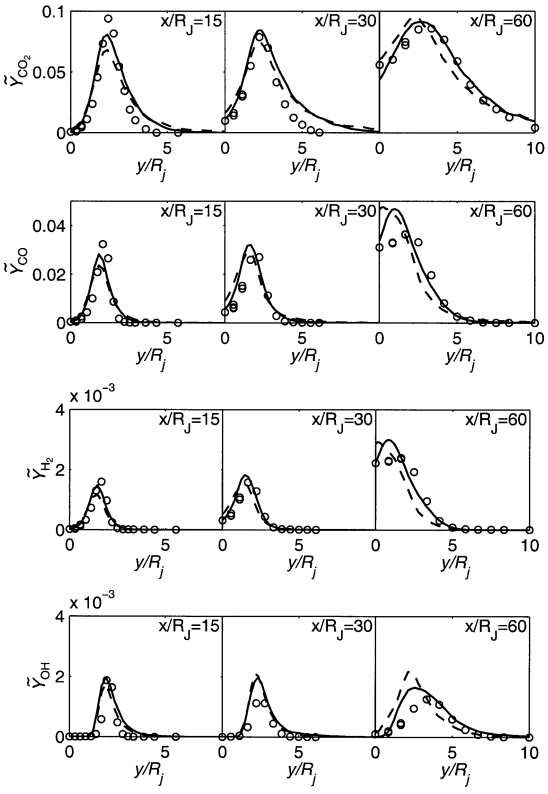

Fig. 4. Radial profiles of flame D (continued). Symbols, experiment; lines: PDF calculations with $C_\phi = 2.0$ (solid), $C_\phi = 1.5$ (dashed).

values of C_ϕ. The lowest value of C_ϕ (i.e., 1.5) leads to the largest values of ξ'' (and also rms of other properties) for $x/R_j \leq 30$. It also implies that decreasing C_ϕ increases not only the variance $\widetilde{\xi''^2}$, but also the scalar flux $\widetilde{v''\xi''}$. Consequently, as may be observed, decreasing C_ϕ also leads to increased spreading of the mean mixture fraction (Figs. 3 and 5).

In general, there is good agreement between the calculations and measurements both in profile shape and peak values. The agreement deteriorates somewhat downstream ($x/R_j = 60$), and for flame F in comparison to flame D. For flame D the difference between the calculations with $C_\phi = 1.5$ and $C_\phi = 2.0$ is not great, and neither value produces uniformly better results. For flame F, the calculations of mean mass fractions with $C_\phi = 1.5$ are clearly superior, resulting in the correct peak levels of most species (with some exceptions at $x/R_j = 60$). The calculations for flame E (not shown)

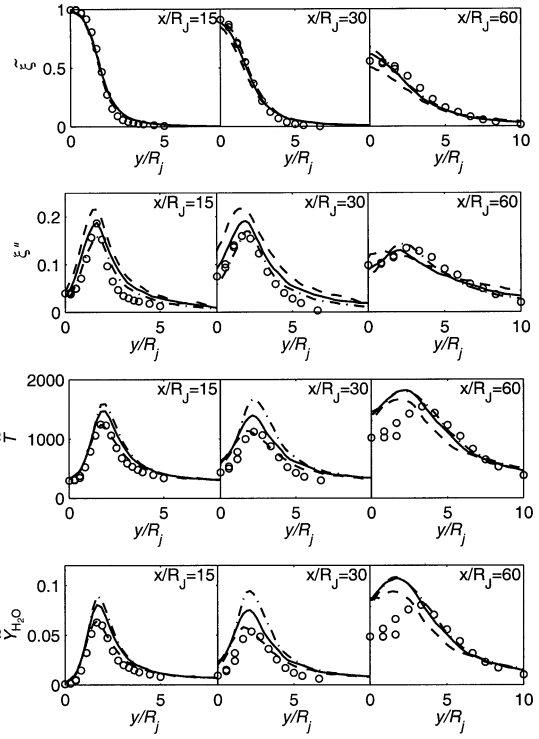

Fig. 5. Radial profiles of flame F. Symbols, experiment; lines: PDF calculations with $C_\phi = 2.0$ (solid), $C_\phi = 1.5$ (dashed), and $C_\phi = 3.0$ (dash-dotted).

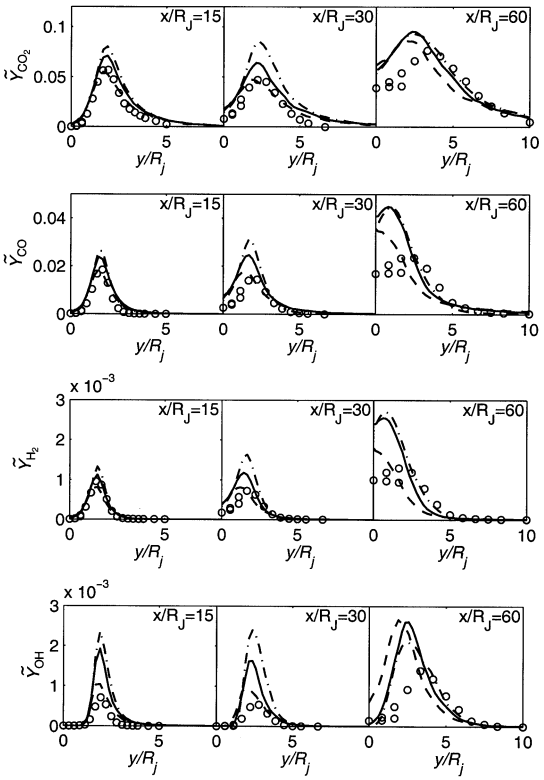

Fig. 6. Radial profiles of flame F (continued). Symbols, experiment; lines: PDF calculations with $C_\phi = 2.0$ (solid), $C_\phi = 1.5$ (dashed), and $C_\phi = 3.0$ (dash-dotted).

show agreement with the data comparable to that for flame D (see [44, 45]).

In flame F, it may be seen (from Fig. 5) that both in the experiment and the calculations the mean temperature at $x/R_j = 60$ is higher than that at $x/R_j = 30$, which indicates the reignition of the flame.

Conditional Statistics of Scalars

Let η be the sample space variable for the mixture fraction ξ; and define the mass-weighted mean of a scalar variable $Y(\mathbf{x}, t)$ conditional on $\xi(\mathbf{x}, t) = \eta$ by $\langle \rho Y(\mathbf{x}, t) | \xi(\mathbf{x}, t) = \eta \rangle / \langle \rho \rangle$. This subsection explores these statistics. At a specified axial location (e.g., $x/R_j = 30$), the estimation of the conditional means uses all particles lying in the single strip of cells in the radial direction centered on that location. Similarly, in the experiment, the conditional means are constructed from data at all radial measurement locations. A total of 50 bins in mixture fraction space are used in the estimation. After the solution reaches statistical stationarity, uniform time-averaging is used to reduce the statistical error.

In Figs. 7–10, the conditional means of temperature and mass fraction of some species for flames D and F are compared at three locations to the experimental data. The most interesting feature of these conditional means is the suppressed values associated with local extinction, which are most evident upstream ($x/R_j \leq 30$) in flame F. It may be observed from Figs. 9 and 10 that these effects are very well represented by the model calculations with $C_\phi = 1.5$: the calculations with $C_\phi = 2.0$ and 3.0 are significantly and uniformly inferior. For the less testing flames D (Figs. 7 and 8) and E (not shown) the agreement is also good, although for several quantities and locations the calculations with $C_\phi = 2.0$ appear superior. The least convincing agreement is for OH, for which (with $C_\phi = 1.5$) the maximum overprediction of the peak value is about 50% (for flame F at $x/R_j = 15$).

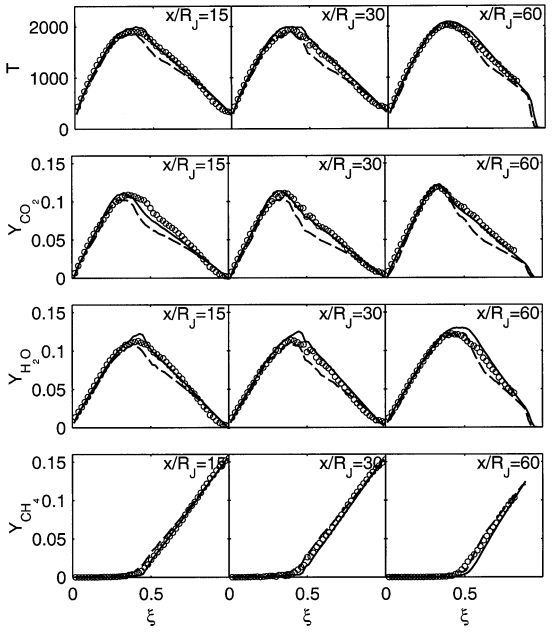

Fig. 7. Conditional means of flame D. Symbols: experiment; lines: PDF calculations with $C_\phi = 2.0$ (solid) and $C_\phi = 1.5$ (dashed).

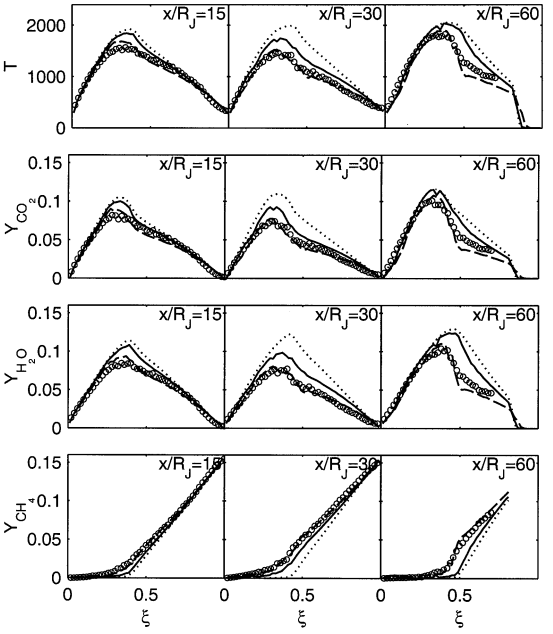

Fig. 9. Conditional means of flame F. Symbols, experiment; lines: PDF calculations with $C_\phi = 2.0$ (solid), $C_\phi = 1.5$ (dashed), and $C_\phi = 3.0$ (dotted).

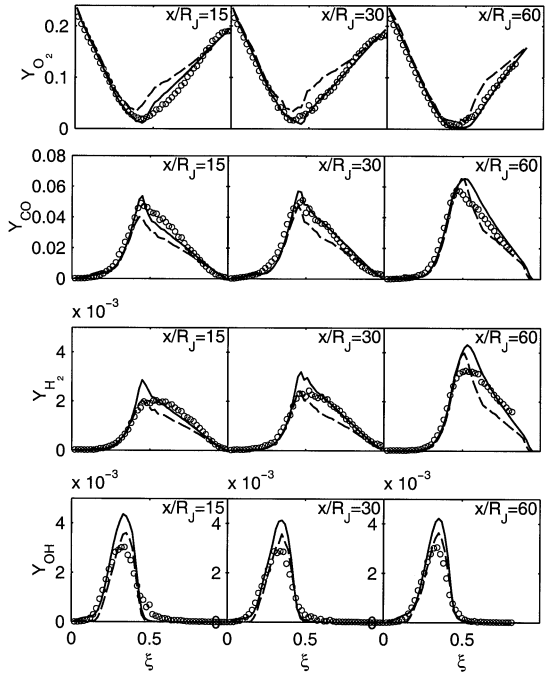

Fig. 8. Conditional means of flame D (continued). Symbols: experiment; lines: PDF calculations with $C_\phi = 2.0$ (solid) and $C_\phi = 1.5$ (dashed).

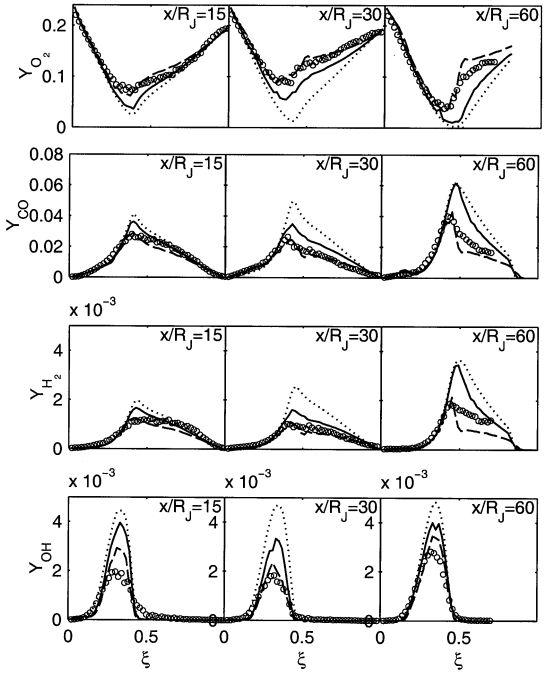

Fig. 10. Conditional means of flame F (continued). Symbols, experiment; lines: PDF calculations with $C_\phi = 2.0$ (solid), $C_\phi = 1.5$ (dashed), and $C_\phi = 3.0$ (dotted).

TABLE 4

Lower (ξ_l) and Upper (ξ_u) Limits of the Mixture Fraction Range Used in the Definition of CPDFs and B.I.; and Reference Mass Fractions (or Temperature) for B.I.

	H_2O	CO_2	CO	OH	H_2	T
ξ_l	0.35	0.30	0.43	0.28	0.48	0.30
ξ_u	0.45	0.40	0.53	0.36	0.58	0.40
$Y_{\|\xi}$ (or $T_{\|\xi}$)	0.1278	0.1127	0.05745	4.527×10^{-3}	3.639×10^{-3}	2023

Conditional PDF

PDFs of scalar fields conditional on the mixture fraction (CPDF) clearly reflect local extinction and reignition processes. Both in PDF calculations and experiments, CPDFs are estimated in a similar manner to the conditional means. However, only samples in a specified mixture fraction range (ξ_l, ξ_u) (different for different quantities) contribute to the estimation of the CPDF. The mixture fraction ranges are specified in accordance to [5], and the values of ξ_l and ξ_u are given in Table 4. The experimental CPDFs shown hereafter are reestimated from the reported individual point measurements, and are different in magnitude from Barlow and Frank's original results which are not correctly normalized. As the main jet velocity is increased in these flames, local extinction is enhanced, which is manifested by the bimodal nature of the CPDFs of temperature and of the major products (CO_2 and H_2O). Particularly in flame F, significant local extinction is observed at $x/R_j = 30$ where the flow is highly strained.

For all three flames (D, E, and F), the CPDFs calculated with $C_\phi = 1.5$ are plotted along with experiments in Figs. 11–16 at $x/R_j = 15$, 30, and 60. It is seen in the experimental data that as the jet velocity increases, the CPDFs of H_2O, CO_2, OH and temperature evolve to manifest bimodal shapes at all three locations: D shows no bimodal shape; E starts to exhibit some; and the bimodal shape is clearly seen in flame F. On the other hand, there exists one peak in the CPDFs of CO and H_2 at $x/R_j = 30$ which shifts to the lower mass fractions of these species as the jet velocity becomes larger. The bimodal shape persists at $x/R_j = 60$ for the temperature, CO_2, OH, and H_2O in flame F, but the median of the CPDFs is located at the higher temperature or mass fraction for $x/R_j = 60$. The bimodal shape also emerges in the CPDFs of CO at $x/R_j = 60$, but the higher mass fraction becomes more probable here than at $x/R_j = 30$. These observations reflect the fact that more local extinction occurs as the jet velocity increases, and that the flame reignites downstream as shown by the higher temperature and the increases in H_2O, CO_2, CO, OH, and H_2 at $x/R_j = 60$.

The calculated CPDFs are in fairly good agreement with experiments: both the shape and the peaks are well captured, and the evolution trend of local extinction with increasing jet velocity is predicted successfully. However, it is noted that the calculation yields relatively narrow shapes of the CPDFs, and the calculated CPDFs of flame D are seen to contain more extinction samples.

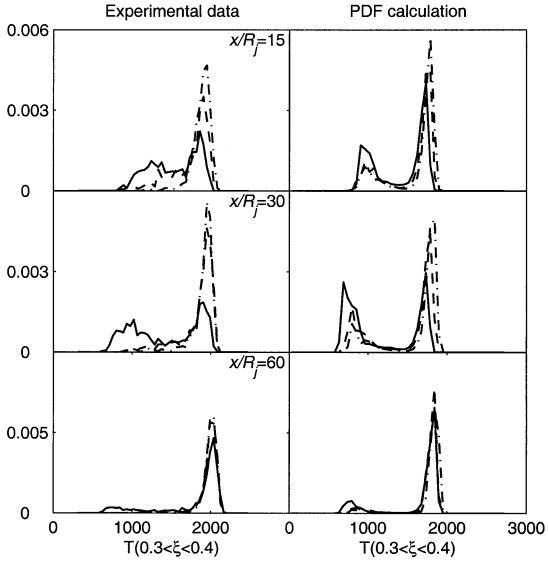

Fig. 11. Conditional PDFs of temperature ($C_\phi = 1.5$). Left are experimental data; right are PDF calculations. Dash-dotted line: flame D; dashed line: flame E; solid line: flame F.

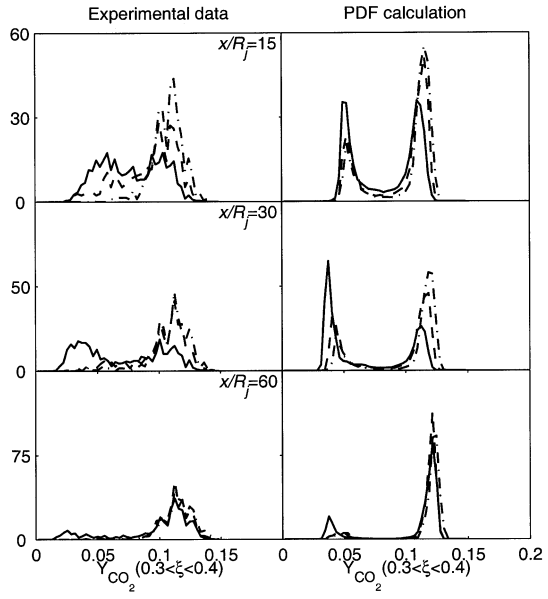

Fig. 12. Conditional PDFs of CO_2 (C_ϕ = 1.5). Left are experimental data; right are PDF calculations. Dash-dotted line: flame D; dashed line: flame E; solid line: flame F.

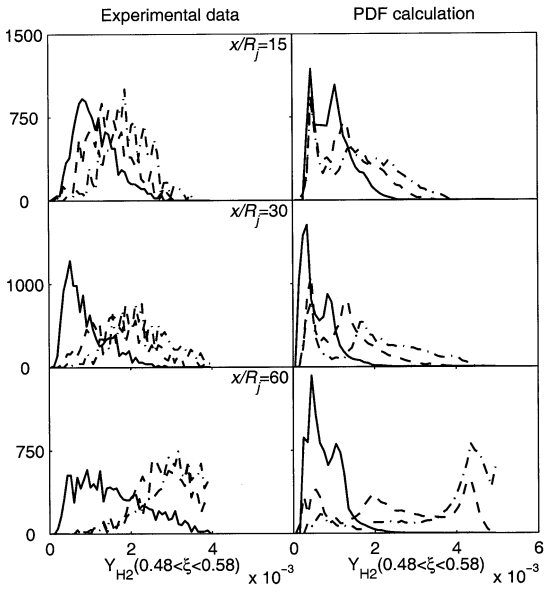

Fig. 14. Conditional PDFs of H_2 (C_ϕ = 1.5). Left are experimental data; right are PDF calculations. Dash-dotted line: flame D; dashed line: flame E; solid line: flame F.

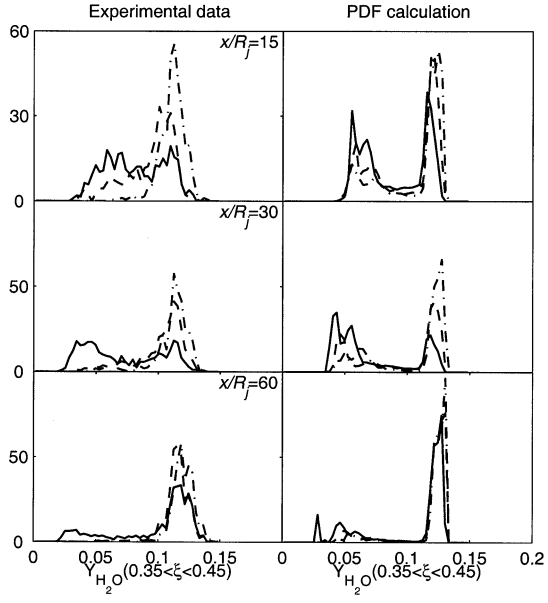

Fig. 13. Conditional PDFs of H_2O (C_ϕ = 1.5). Left are experimental data; right are PDF calculations. Dash-dotted line: flame D; dashed line: flame E; solid line: flame F.

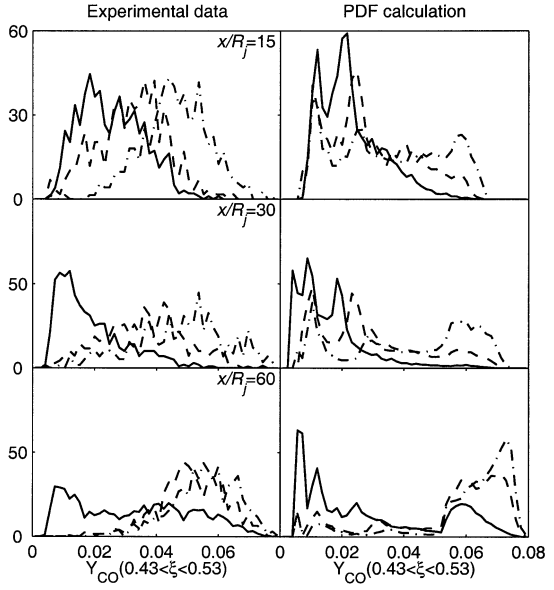

Fig. 15. Conditional PDFs of CO (C_ϕ = 1.5). Left are experimental data; right are PDF calculations. Dash-dotted line: flame D; dashed line: flame E; solid line: flame F.

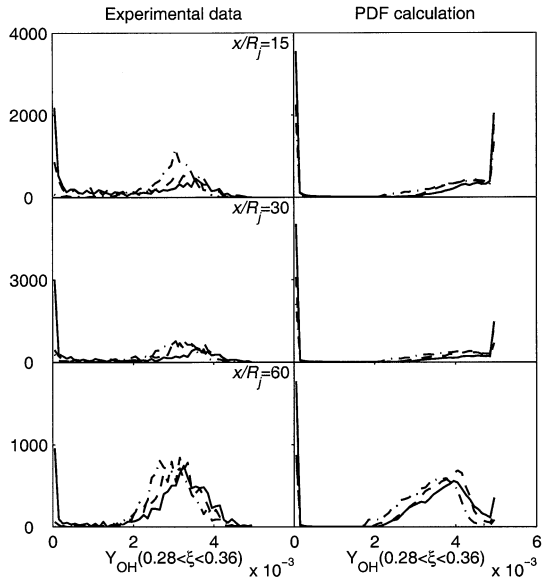

Fig. 16. Conditional PDFs of OH (C_ϕ = 1.5). Left are experimental data; right are PDF calculations. Dash-dotted line: flame D; dashed line: flame E; solid line: flame F.

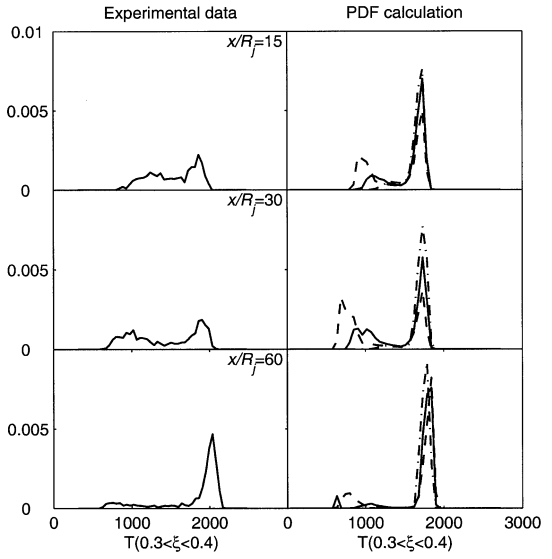

Fig. 17. Conditional PDFs of flame F. Left are experimental data; right are PDF calculations with C_ϕ = 2.0 (solid), C_ϕ = 1.5 (dashed), and C_ϕ = 3.0 (dash-dotted).

Calculations with C_ϕ = 2.0 (not shown) indicate that the agreement of flame D and E results with the data appears better than that obtained with C_ϕ = 1.5. The above observations imply that C_ϕ = 1.5 tends to give a distribution more probable to the lower mass fraction and temperature, and thus brings about more local extinction.

For flame F, further comparisons of the CPDFs of temperature, CO_2, and CO are plotted in Figs. 17–19 for different model values of the constant C_ϕ. Again, it may be seen that the value C_ϕ = 1.5 leads to the greatest amount of local extinction in this flame; and it appears that C_ϕ = 1.5 gives the best agreement to the experiment for this flame. The sensitivity of the CPDFs to the choice of C_ϕ is particularly evident for CO at x/R_j = 30 (Fig. 19).

Scatter Plots

Figures 20–25 show scatter plots of T, OH, and CO versus mixture fraction ξ for flames D and F. (Not shown are scatter plots for CO_2 and H_2O which are similar to those of T, and for H_2 which is similar to that of CO.) The calculations are performed with C_ϕ = 1.5. In the plots of both the experimental and calculated data, the composition of a strained (a = 100 s^{-1}) laminar flame is shown (as a solid line, [47]) for reference.

While these plots are informative, it should be appreciated that there are limitations in making quantitative comparisons between the

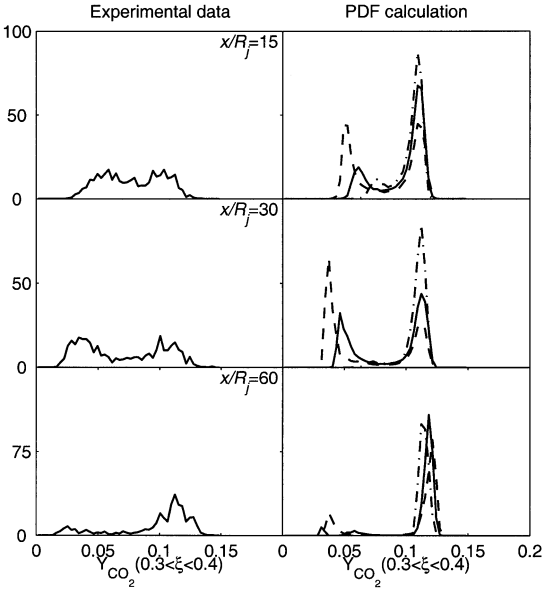

Fig. 18. Conditional PDFs of flame F. Left are experimental data; right are PDF calculations with C_ϕ = 2.0 (solid), C_ϕ = 1.5 (dashed), and C_ϕ = 3.0 (dash-dotted).

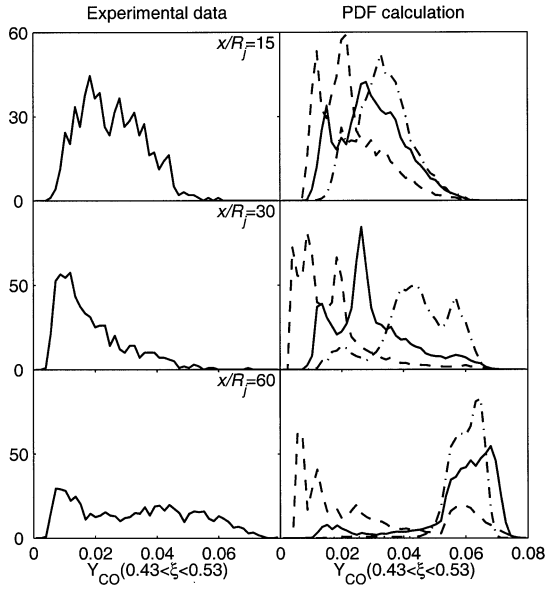

Fig. 19. Conditional PDFs of flame F. Left are experimental data; right are PDF calculations with $C_\phi = 2.0$ (solid), $C_\phi = 1.5$ (dashed), and $C_\phi = 3.0$ (dash-dotted).

experiments and the calculations. Some considerations in this regard are:

1. The experimental plots contain data from different radial locations. These locations, and the number of samples obtained from each, are not reported.
2. In the calculations the particles have different numerical weights, but these weights are not distinguished on the scatter plots. Also, only a subset of particles from the calculations are plotted.
3. Especially in the calculations, many points may have the same values, which is not evident in the plots. (For example in Fig. 24 many samples correspond to $Y_{OH} = 0$.)

For flame D, there is generally good comparison between the calculations and experiments, but with the former suggesting a greater amount of local extinction.

For flame F, the bimodal nature of the CPDF of temperature at $x/R_j = 30$ is clearly evident in the calculated scatter plot (Fig. 23): there is an upper band (for lean mixtures) close to the flamelet line, and a lower band with a peak temperature of around 1000 K at stoichiometric. At $x/R_j = 60$, the calculated scatter plot of T exhibits a characteristic banded shape which can be described as a triangle with two legs. The near void in the center of the triangle is in agreement with the experimental data. Excluding the points near the flamelet line, the scatter plots appear as three bands emanating symmetrically from their intersection around $\xi_s = 0.351$. The experimental data show no such structure: it is most likely a manifestation of the "stranding" phenomenon connected with the EMST model.

It is interesting to observe that for very lean mixtures ($\xi < 0.2$) the experimental values of Y_{CO} (Fig. 25) are significantly above the flamelet line. This feature is captured by the calculations.

Burning Index

It is desirable to characterize local extinction (or the lack thereof) quantitatively by a single variable. A particle or sample is declared to be in the burning mode when it is near the state of a strained laminar flame. Here we introduce the *burning index* (B.I.) to characterize the lack of local extinction: it is defined as

$$\text{B.I.} \equiv Y_{|\xi}/Y_r, \tag{14}$$

where $Y_{|\xi}$ denotes the first moment of the CPDF of a selected species, and Y_r is a reference mass fraction which is taken to be the peak value of the mass fraction of the species based on a strained, opposed-flow laminar flame calculation with a strain parameter $a = 100\ \text{s}^{-1}$ [47]. The reference values for different species are listed in Table 4. Note that $Y_{|\xi}$ is the mass-weighted conditional mean

$$Y_{|\xi} = \frac{\langle \rho Y | \xi_l \le \xi < \xi_u \rangle}{\langle \rho | \xi_l \le \xi < \xi_u \rangle}. \tag{15}$$

By definition, higher values of B.I. correspond to a near complete burning, whereas lower values of B.I. imply incomplete burning or extinction. The B.I. for temperature is defined similarly as the mass-weighted conditional mean of temperature divided by T_r.

First the burning indices based on H_2O, CO_2, CO, OH, H_2, and temperature are plotted in Fig. 26 versus the jet bulk velocity at $x/R_j = 30$ where the amount of local extinction is the highest. It is clear that the burning index de-

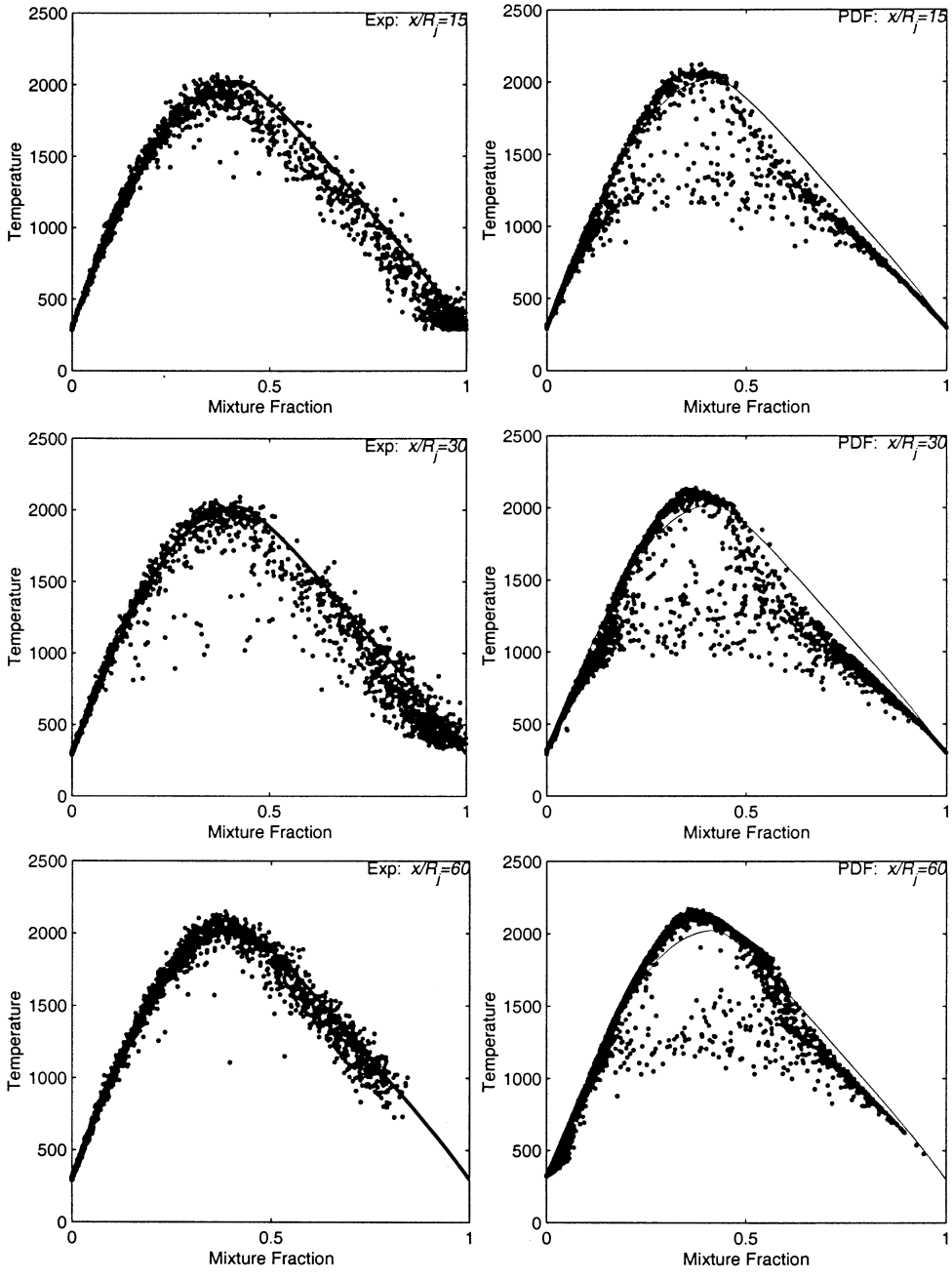

Fig. 20. Scatter plot of temperature against mixture fraction of flame D at x/R_j = 15, 30, and 60: left, experimental data; right, PDF calculations (C_ϕ = 1.5); lines, strained laminar flame (a = 100 s^{-1}).

creases as the jet bulk velocity is increased. This is consistent with the experimental observation that flame D exhibits very little extinction, whereas flame F has the most local extinction. The PDF calculations predict this trend very well. (It should be noted that in addition to the larger inlet velocities, flame F differs from flames D and E in having a slightly lower pilot temperature at inlet.)

To quantify the extinction and reignition in the flame straightforwardly, the B.I.'s are compared for flames D, E, and F at different axial

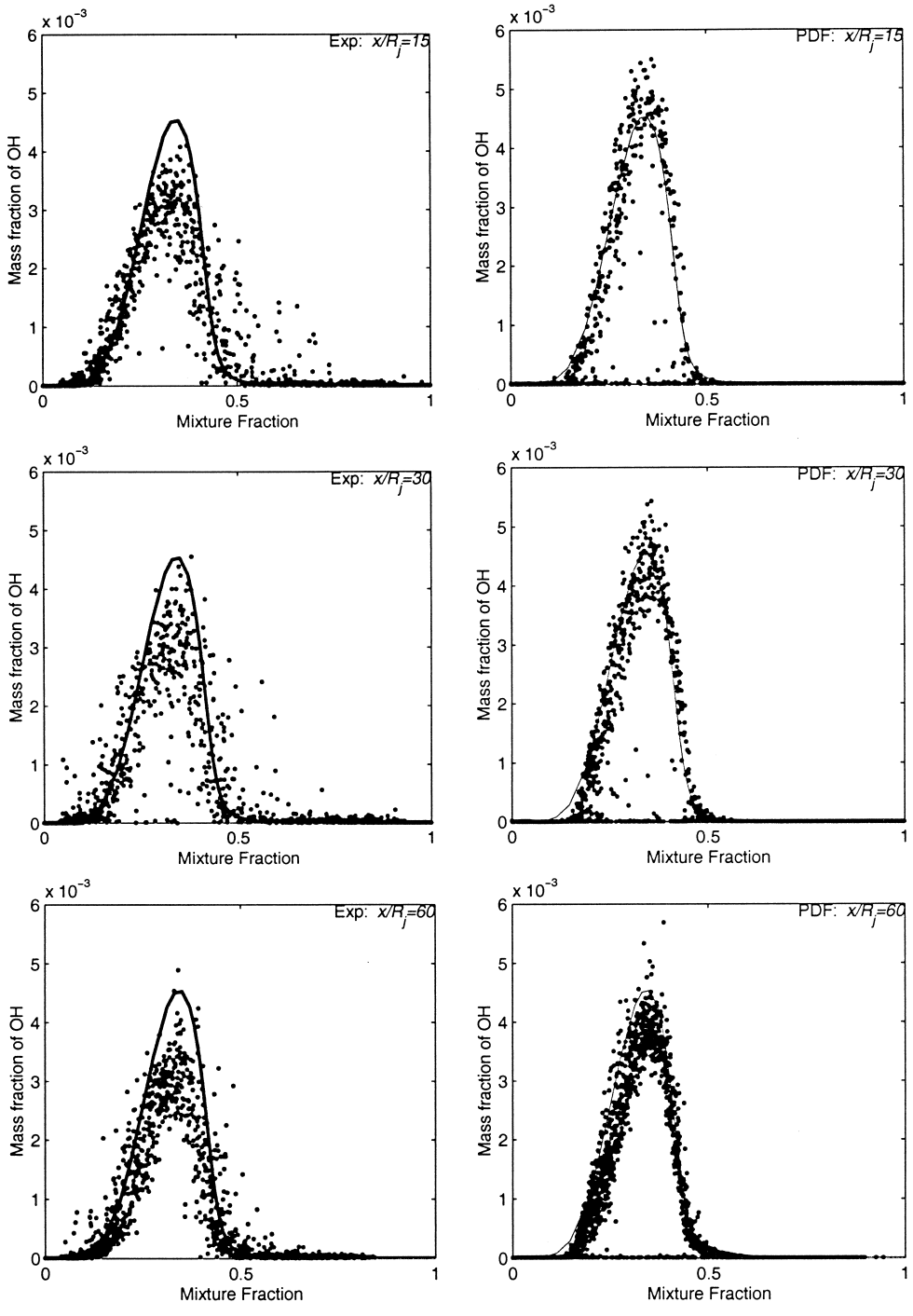

Fig. 21. Scatter plot of OH against mixture fraction of flame D at $x/R_j = 15$, 30, and 60: left, experimental data; right, PDF calculations ($C_\phi = 1.5$); lines, strained laminar flame ($a = 100\ \mathrm{s}^{-1}$).

locations in Fig. 27. The PDF calculations use $C_\phi = 1.5$. It is seen again that as the jet velocity increases, the B.I.'s decrease, indicating more local extinction. The B.I.'s of flame D based on H_2O, CO_2, OH, and temperature show little variation upstream to downstream, whereas in

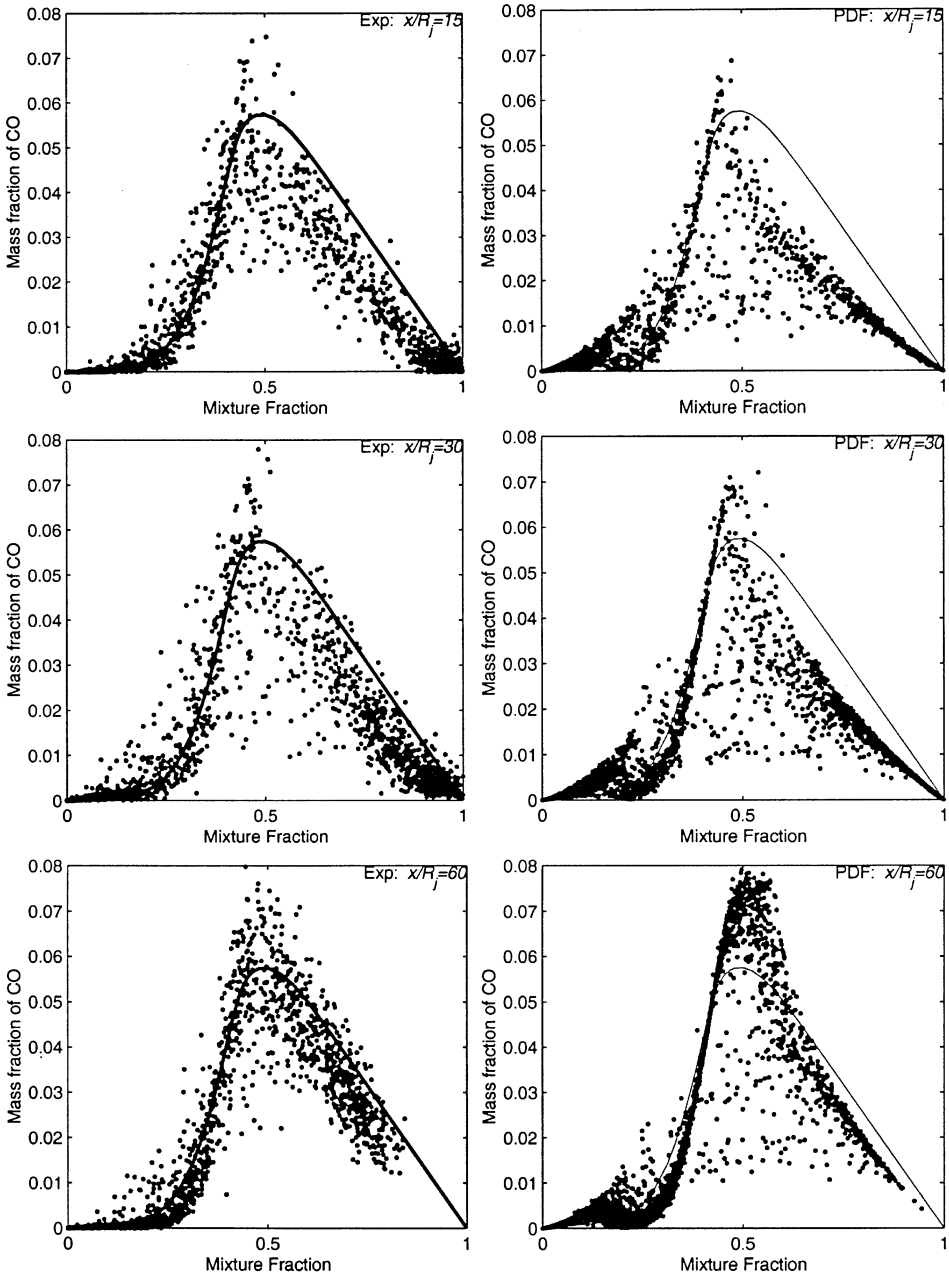

Fig. 22. Scatter plot of CO mass fraction against mixture fraction of flame D at $x/R_j = 15$, 30, and 60: left, experimental data; right, PDF calculations ($C_\phi = 1.5$); lines, strained laminar flame ($a = 100\ \mathrm{s}^{-1}$).

flame F, it is observed that in the experiments the lowest B.I. occurs at $x/R_j = 15$ and 30. At $x/R_j = 60$, B.I. is recovered gradually, and reaches to the maximum value at $x/R_j = 90$ where the flame is nearly fully reburnt except for OH. Thus, B.I. is indeed a good quantity measuring the extent of local extinction and reignition in these piloted-jet flames. The calculated B.I.'s are in very good agreement with the experimental data.

Along with the experimental data, the B.I.'s of calculations for flame F with four values of C_ϕ are also plotted in Fig. 28. The PDF calculations with $C_\phi = 1.5$ and $C_\phi = 2.0$ exhibit the

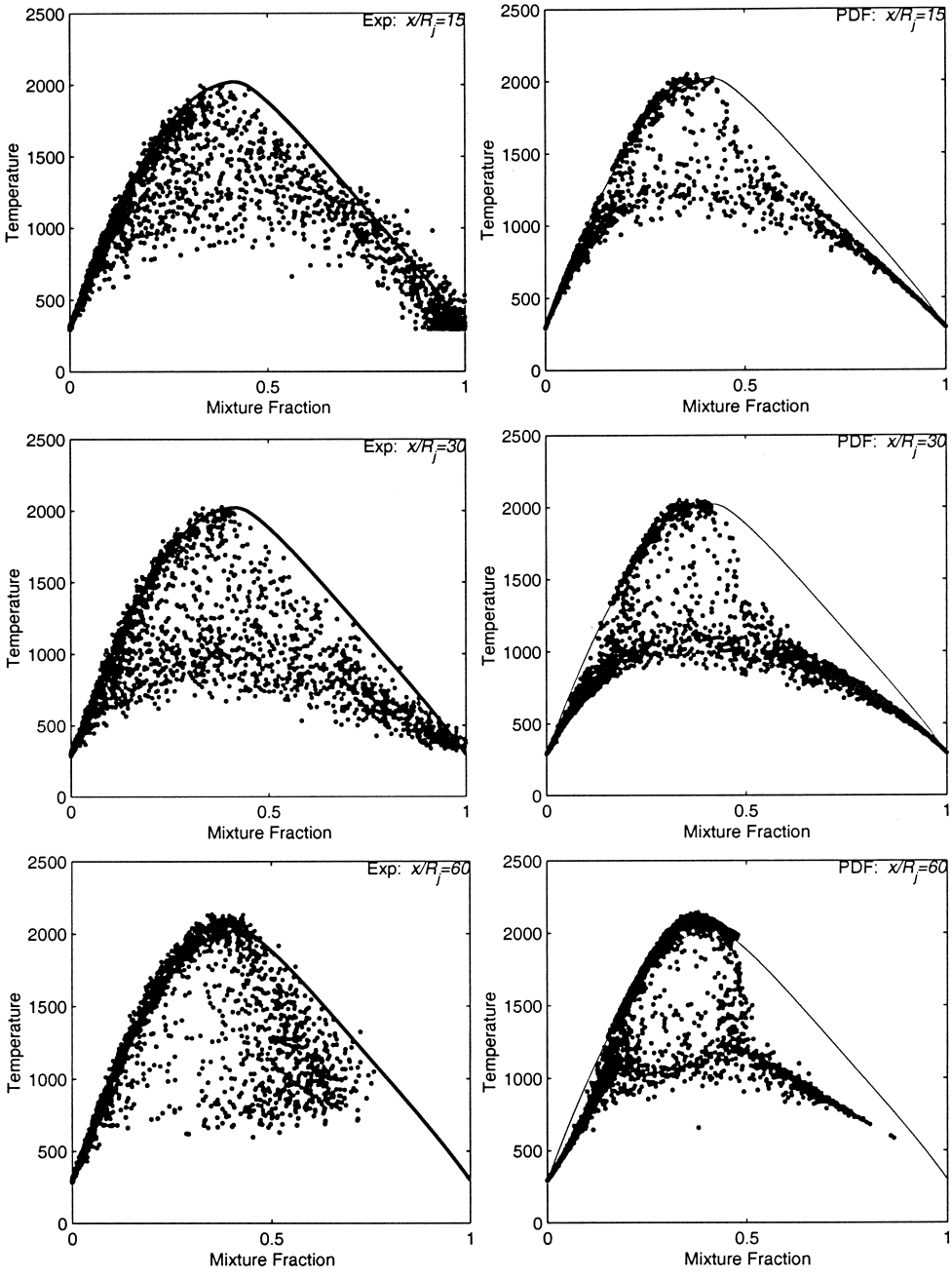

Fig. 23. Scatter plot of temperature against mixture fraction of flame F at $x/R_j = 15$, 30, and 60: left, experimental data; right, PDF calculations ($C_\phi = 1.5$); lines, strained laminar flame ($a = 100\ \mathrm{s}^{-1}$).

similar behavior of B.I. along the axial direction, and in particular the results with $C_\phi = 1.5$ match the experimental data remarkably well (except for the B.I.'s based on H_2 and CO species downstream). For $C_\phi = 3.0$, little local extinction is predicted, whereas $C_\phi = 2.0$ yields the correct trend of local extinction and reignition, but relatively lower amounts of extinction than that observed in the experiment. A further decrease of C_ϕ to $C_\phi = 1.0$ gives rise to even more extinction, and the B.I. based on CO shows almost no reignition downstream.

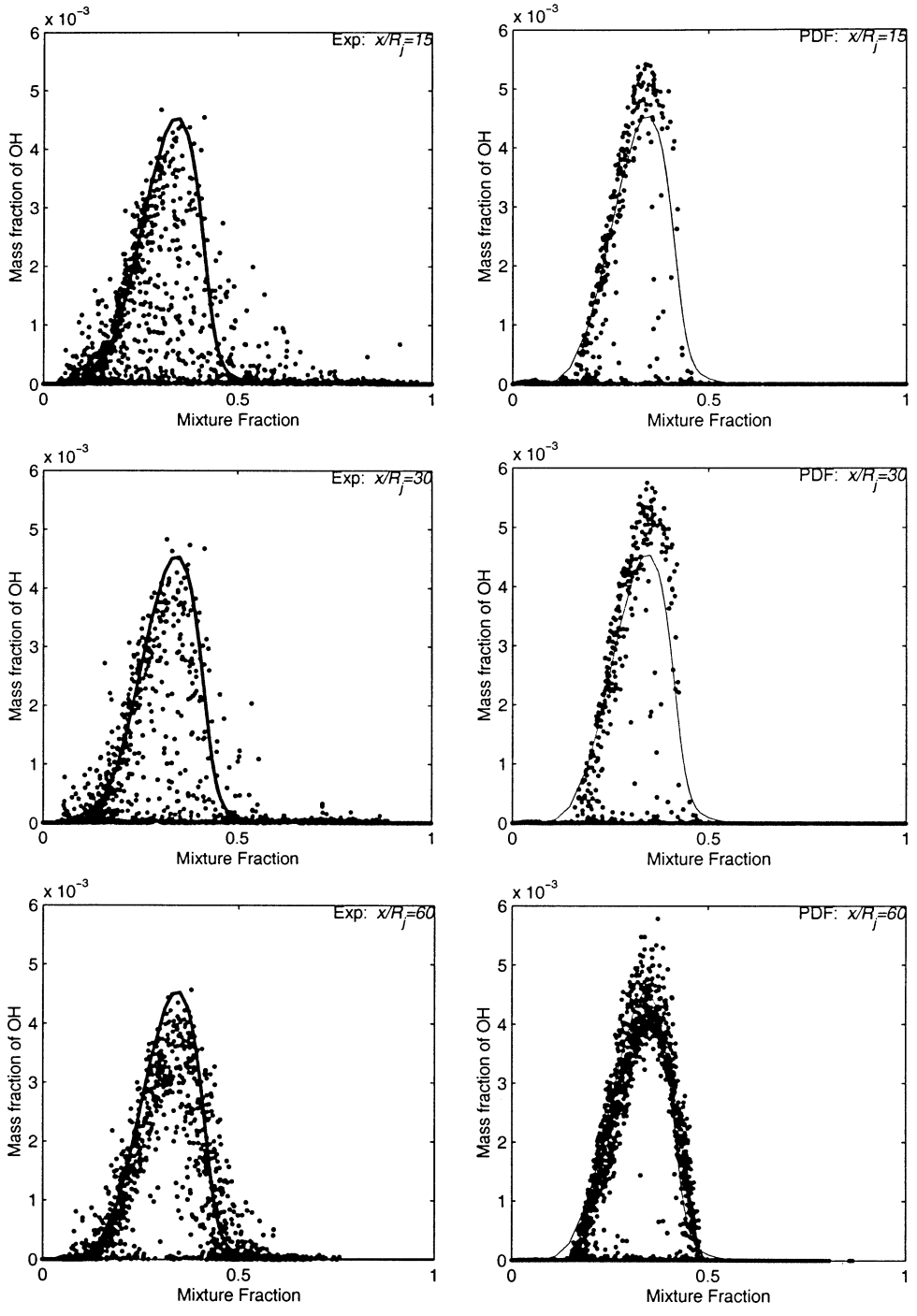

Fig. 24. Scatter plot of OH against mixture fraction of flame F at x/R_j = 15, 30, and 60: left, experimental data; right, PDF calculations (C_ϕ = 1.5); lines, strained laminar flame (a = 100 s^{-1}).

DISCUSSION

Generally, the calculated mean and variance profiles of velocity and mixture fraction are in good agreement with the experimental data. Also, the comparison of radial mean profiles of other scalars with the experiment is rather satisfactory. It is shown in the mean profiles

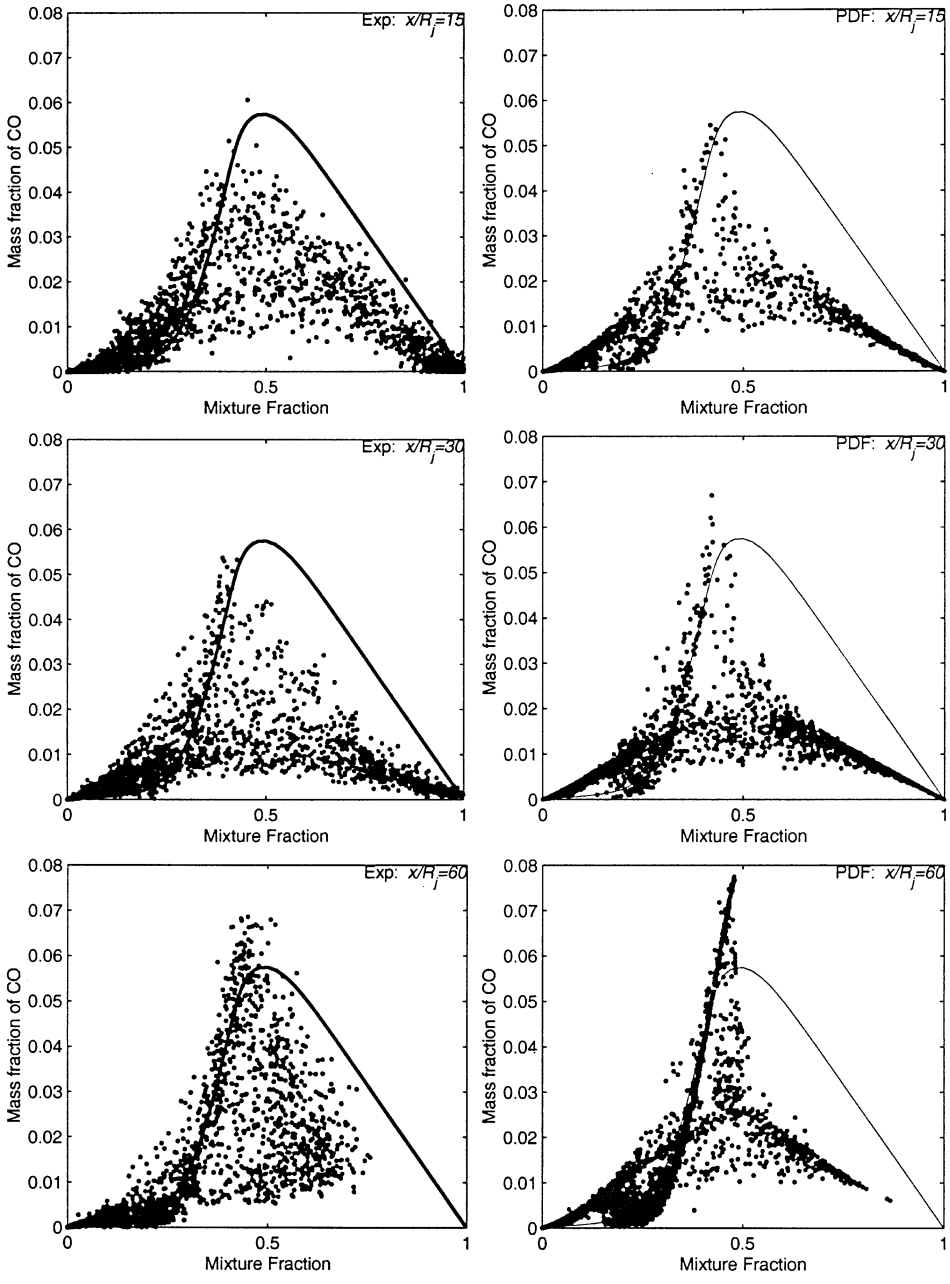

Fig. 25. Scatter plot of CO mass fraction against mixture fraction of flame F at $x/R_j = 15$, 30, and 60: left, experimental data; right, PDF calculations ($C_\phi = 1.5$); lines, strained laminar flame ($a = 100\ \mathrm{s}^{-1}$).

(through varying the mixing model constant C_ϕ) that $\langle\rho\rangle$ has a significant effect on $\tilde{U}$. The velocity model adopted is SLM. It is expected that the use of a more advanced velocity model, e.g., the Lagrangian Isotropization of Production Model (LIPM) with pressure transport model [9, 10, 29], can improve the prediction of velocity fields. Also, the effects of variable density on the velocity model need to be investigated [33].

The scalar means conditional on the mixture fraction in flame D are not far from mildly strained flamelet values, but those in F possess lower values for T and products, indicative of

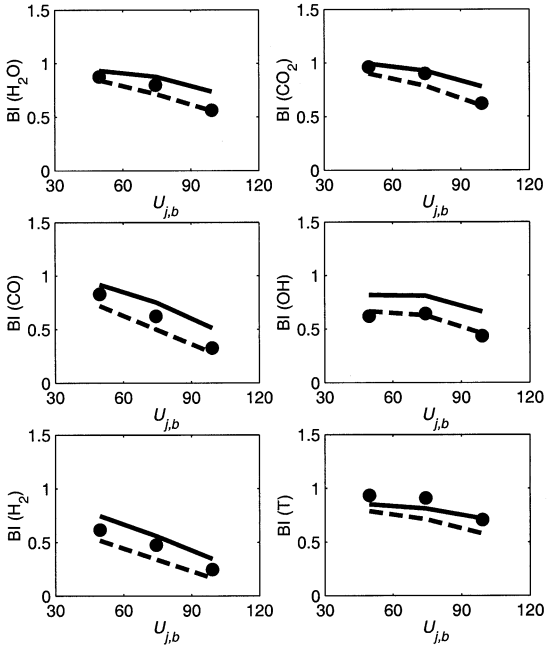

Fig. 26. Burning indices vs. jet velocities ($x/R_j = 30$). Filled symbols: experiments; lines: PDF calculations with $C_\phi = 2.0$ (solid) and $C_\phi = 1.5$ (dashed).

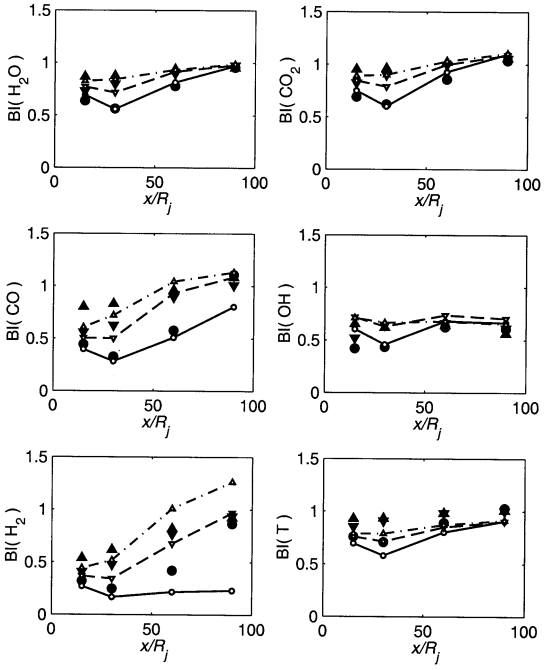

Fig. 27. Burning indices of flames D, E, and F. Filled symbols: experiments; lines with empty symbols are PDF calculations with $C_\phi = 1.5$. Circle and solid line, flame F; down-triangle and dashed line, flame E; up-triangle and dash-dotted line, flame D.

finite-rate chemistry. Comparing to the work of Saxena and Pope [22], the same velocity model, the mixing model, and a very similar turbulence frequency model are used, and yet the flames calculated in this work are much more difficult because of the presence of local extinction in these flames, in particular in flame F. The only significant difference in the models is the chemistry mechanism: a C_1 skeletal mechanism is used in the previous calculations. The predicted conditional mean of CO for $\xi > \xi_s$ in those calculations is about twice higher than the experimental data, whereas in the current calculations the composition of CO (even for $\xi > \xi_s$) is shown to agree to the experiment very well for all three flames. This observation demonstrates that ARM removes the deficiencies of the skeletal mechanism since it includes some C_2 species in the mechanism. This is also observed in [27].

The evolution of local extinction in three flames is well represented by the conditional PDFs of various species. To quantify the extent of local extinction (or the lack of local extinction), the burning index is introduced. Both the experiments and the calculations show that this index is a good measure of the lack of local extinction: it indeed clearly depicts the evolution of the extent of extinction with increasing jet velocity, and also reflects the axial variation of local extinction and reignition in the flame. The comparisons of CPDFs and B.I.'s between calculations and experiments are very encouraging. Notably, in flame F, the bimodal nature of CPDFs which symbolizes strong local extinction is successfully captured by the present calculations. On the other hand, the calculated B.I.'s also show the same evolutions of local extinction and reignition as the experimental data, and their values are in good agreement with the experimental data. Note that only when the details of turbulence and finite-rate chemistry interaction are described accurately, can these local extinction and reignition processes (particularly in flame F) be resolved. Also, the current calculations do not use any artificial treatment to stabilize the flame. Therefore, the present results essentially demonstrate that the joint velocity–composition–frequency PDF model with the EMST mixing model represents

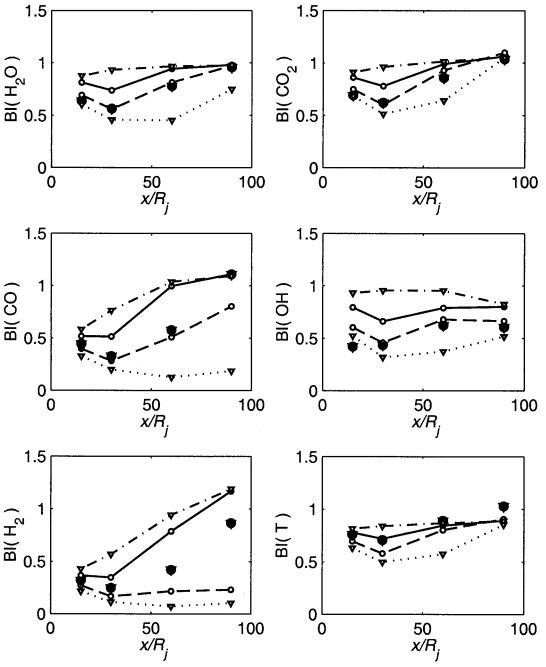

Fig. 28. Burning indices of flame F. Filled symbols: experiments; lines with empty symbols are PDF calculations with $C_\phi = 2.0$ (solid), $C_\phi = 1.0$ (dotted), $C_\phi = 1.5$ (dashed), and $C_\phi = 3.0$ (dash-dotted).

well the intense interaction between turbulence and finite-rate chemistry.

The comparison of conditional means, CPDFs, and B.I.'s with different values of the model constant C_ϕ shows that this constant has a major impact on the results. It is evident that the prediction of local extinction is sensitive to the value of C_ϕ. One critical observation is that in these flames, reducing C_ϕ leads to higher intensity of local extinction. This is also observed in the PDF calculations with the IEM mixing model [19] as well as the modified Curl's mixing model [18]. It is implied that increasing C_ϕ causes the mixture to become more effectively homogenized, and thus leads the combustion to approach to chemical equilibrium faster. In flame F, $C_\phi = 1.5$ gives better results for conditional means in comparison with the experimental data at locations $x/R_j = 15$ and 30 where the strongest local extinction is present. Also, at these locations by changing $C_\phi = 2.0$ to 1.5, the model shifts the CPDFs to lower values, and thus leads to lower B.I.'s which are also in better agreement with experimental data.

In discussing local extinction it is natural to

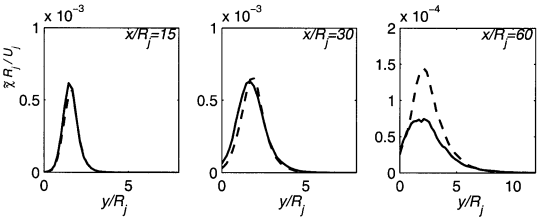

Fig. 29. Radial profiles of normalized mean scalar dissipation $\tilde{\chi}R_j/U_j$ for flame F. Solid line: $C_\phi = 1.5$; dashed line, $C_\phi = 2.0$.

consider the scalar dissipation χ. According to the model, the mean scalar dissipation is

$$\tilde{\chi} = \frac{\widetilde{\xi''^2}}{\tau_\phi} = C_\phi \Omega \widetilde{\xi''^2}. \tag{16}$$

Increasing C_ϕ causes $\widetilde{\xi''^2}$ to decrease, so the overall effect on $\tilde{\chi}$ is not obvious. For flame F, Fig. 29 shows the calculated radial profiles of $\tilde{\chi}$ for $C_\phi = 1.5$ and 2.0. Interestingly, it may be seen that at $x/R_j = 15$ and 30 $\tilde{\chi}$ is essentially the same for the two different values of C_ϕ. Hence, at these locations, the increased local extinction observed with $C_\phi = 1.5$ (compared to $C_\phi = 2.0$) is not attributed to higher scalar dissipation. Furthermore, at $x/R_j = 60$, Fig. 29 shows that with $C_\phi = 1.5$ the scalar dissipation is reduced (compared to $C_\phi = 2.0$), and yet Fig. 28 shows that the local extinction is increased. It appears, therefore, that the dominant effect of increasing C_ϕ is to decrease the scalar variance which in turn reduces the amount of local extinction.

The sensitivity to C_ϕ indicates also the importance of mixing, and hence of the mixing model. We attempted to make calculations of these flames with the IEM mixing model and the ARM for methane, but failed to obtain stable flames. In future work it would be of interest to investigate the performance of the modified Curl mixing model. Lindstedt et al. [28] showed that with a detailed chemistry mechanism it is possible to obtain stable combustion for flame F without artificial ignition. The present calculations, however, use the EMST mixing model for which an important feature is the localness of mixing. With the use of this mixing model, the calculations successfully yield the stabilized flame even for flame F. The present results

(especially for flame F) tend to favor $C_\phi = 1.5$ for the EMST mixing model (although some results with $C_\phi = 2.0$ are superior for flames D and E).

The traditional value of C_ϕ is 2.0. It is noted, however, that the measurement of a helium round jet in air by Panchapakesan and Lumley [39] implies the value $C_\phi = 1.5$. In addition, as discussed by Peters [48], there are arguments, originally advanced by Corrsin [49], which suggest that C_ϕ is smaller for reactive scalars.

The current calculations use about 100 particles in each cell with 3600 cells in the domain $(120,25)R_j$. However, the improvement of numerical accuracy downstream ($x/R_j \geq 90$) is desired. It is recognized that the bias in the current algorithm is relatively large [10]. To reduce the bias, one basically needs to use a larger number of particles (say 400 particles per cell), but this costs much more computational work. In the present case, that means at least 400 hours CPU time per processor with a total of 5 processors for one calculation, which appears not practical (using more processors reduces the parallel efficiency). A recent development of the consistent hybrid particle/finite volume scheme seems promising in reducing the bias, and improving the computational efficiency [50]. The computational efficiency can also be improved significantly by employing a parallel implementation of ISAT. In a typical calculation of this study, the ISAT calculation takes about 90% of the total CPU time of which perhaps 95% is spent on building the ISAT table. By the parallel calculation of ISAT, the task of building table can be shared by all processors, thus accelerating the calculation. In previous PDF/ISAT calculations of piloted-jet flames the speed-up factor achieved by ISAT is about 40 [22, 27]. The speed-up factor for these calculations is not known.

In comparison to previous PDF calculations, the success of the present calculations stems from the combined use of the EMST mixing model and the ARM for methane. Other important ingredients are an accurate and well-characterized particle/mesh method and the ISAT algorithm. Without any one of these four ingredients, accurate calculations of the details of the turbulence–chemistry interactions would not have been possible.

It is also interesting to note the ingredients that the current model does not contain—for it may be supposed that such missing ingredients are not essential. There is no explicit representation of the micro-structure, as for example in a flamelet model. The model does not involve any molecular transport properties (diffusivity, thermal conductivity, or viscosity); and takes no account of differential diffusion. The molecular mixing is modeled to occur at the mean rate $C_\phi\Omega$: mixing-rate fluctuations are not explicitly included.

CONCLUSIONS

In this paper, the joint velocity–composition–turbulence frequency PDF model is used to calculate a series of turbulent nonpremixed methane piloted-jet flames, namely flames D, E, and F of Barlow and Frank [5]. The model incorporates the EMST mixing model and the ARM for methane oxidation. The ARM is implemented via the ISAT algorithm. Comprehensive comparisons of basic characteristics of the flames—scalar statistics conditional on mixture fraction, scalar PDFs conditional on mixture fraction, scatter plots, and B.I.'s—between measurements and calculations are conducted to ascertain the capability and accuracy of the present model to describe the strong turbulence and finite-rate chemistry interaction. Conclusions are drawn as follows:

The numerical accuracy of the calculations has been thoroughly assessed [44, 45], and is sufficient to test the model performance in the regions of the flames that exhibit local extinction and reignition. The numerical errors in mean and rms profiles are around 10% for $x/R_j \leq 30$, less than 20% at $x/R_j = 60$, but are larger at $x/R_j \geq 90$ and for Reynolds stresses. Statistics conditional on mixture fraction show considerably less numerical error. (More accurate and efficient numerical algorithms are currently being developed which are expected to yield numerically accurate calculations for the full extent of the flame at reasonable computational cost.)

In the calculations, stabilized flames are obtained successfully for all three flames without introducing any special treatment that has been

found necessary in some previous calculations [28]. This success is attributed to the localness of the EMST mixing model. The sensitivity of the calculations to the EMST model coefficient C_ϕ is also investigated. Increasing C_ϕ yields combustion closer to equilibrium. Generally, the results with $C_\phi = 1.0$ and 3.0 are poor, whereas $C_\phi = 1.5$ tends to produce the right amount of local extinction, in good agreement with the experiments. The optimal value of C_ϕ is likely in the range from 1.5 to 2.

The calculated scalar means conditional on mixture fraction are in good agreement with experimental data. The ARM mechanism for methane appears to remedy the deficiencies of the skeletal mechanism used in previous calculations. In particular, the prediction of CO for $\xi > \xi_s$ is significantly improved. This is due to the inclusion of some C_2 species in the development of the ARM from the GRI mechanism. However, the OH mass fraction tends to be overpredicted, by as much as 50% in the worst case.

As the main jet velocity increases, the amount of local extinction increases. In particular, flame F has substantial local extinction while it reignites downstream. Aiming at quantifying the local extinction and reignition phenomena, we introduce a single variable BI (Burning Index). It proves to be a good measure of the lack of local extinction (or the burning mode of a flame). The calculated B.I.'s not only reveal the same evolution as that by the experiments, but also agree quantitatively very well to the experimental data. From the comparisons of the B.I.'s as well as the CPDFs, the present model proves to capture successfully the features of local extinction and reignition.

The chemical reaction is implemented by the ISAT algorithm. With this algorithm, accurate calculations of major and minor species are accomplished with a manageable computational cost. However, it is desirable to improve the computational efficiency through implementing the parallel computation of ISAT. Currently, the EMST mixing model is parallelized in the *PDF2DV* code, whereas the ISAT algorithm has not been fully parallelized. About 90% of the total CPU time is spent on the ISAT calculation, and of which the table building takes about 95% time. The parallel implementation can significantly improve the computational efficiency by sharing the time of building the ISAT table over parallel nodes.

To conclude, the PDF/ISAT method has been demonstrated to be capable of representing the intense interaction between turbulence and finite-rate chemistry in turbulent nonpremixed flames. However, it is realized that further improvements in submodels (e.g., the velocity model), and especially in the computational efficiency are desirable.

This work was supported in part by Air Force Scientific Office of Research Grant F49620-97-1-0126, and in part by the U.S. Department of Energy, Federal Energy Technology Center under cooperative agreement No. DE-FC21-92-MC29061 through the Advanced Gas Turbine Systems Research (AGTSR) program. Some computations were performed on the Cornell Theory Center's supercomputers, which receives funding from Cornell University, New York State, and members of the Center's Corporate Partnership Program. For useful comments on a draft of this paper, we are grateful to Professors R. W. Bilger, G. Kosály, A. R. Masri, and N. Peters.

REFERENCES

1. Libby, P. A., and Williams, F. A. in *Turbulent Reacting Flows* (P. A. Libby and F. A. Williams, Eds.) Academic Press, London 1994, p. 1.
2. Peters, N., *Twenty-First Symposium (International) on Combustion*, 1988, p. 1231.
3. Pope, S. B., *Prog. Energy Combust. Sci.* 11:119 (1985).
4. Bilger, R. W., *Phys. Fluids A* 5:436 (1993).
5. Barlow, R. S., and Frank, J. H., *Twenty-Seventh Symposium (International) on Combustion*, The Combustion Institute, Pittsburgh, 1998, p. 1087.
6. Masri, A. R., and Bilger, R. W., *Twenty-First Symposium (International) on Combustion*, The Combustion Institute, Pittsburgh, 1988, p. 1511.
7. Masri, A. R., Dibble, R. W., and Barlow, R. S., *Prog. Energy Combust. Sci.* 22:307 (1996).
8. *Third International Workshop on Measurement and Computation of Turbulent Nonpremixed Flames*, Boulder, CO, 1998.
9. Van Slooten, P. R., Jayesh, and Pope, S. B., *Phys. Fluids* 10:246 (1998).
10. Xu, J., and Pope, S. B., *J. Comput. Phys.* 152:192 (1999).
11. Subramaniam, S., and Pope, S. B., *Combust. Flame* 115:487 (1998).
12. Sung, C. J., Law, C. K., and Chen, J.-Y., *Twenty-*

Seventh Symposium (International) on Combustion, Pittsburgh, The Combustion Institute, 1998, p. 295.
13. Pope, S. B., *Combust. Theo. Modelling* 1:41 (1997).
14. Pope, S. B., Unpublished, Cornell University, 1994.
15. Hinz, A., Hassel, E. P., and Janicka, J., Third International Workshop on Measurement and Computation of Turbulent Nonpremixed Flames, Boulder, CO, 1998.
16. Barlow, R. S. (1998). http://www.ca.sandia.gov/tdf/Workshop.html
17. Bilger, R. W., Starner, S. H., and Kee, R. J., *Combust. Flame* 81:411 (1990).
18. Chen, J. Y., Kollmann, W., and Dibble, R. W., *Combust. Sci. Technol.* 64:315 (1989).
19. Jones, W. P., and Kakhi, M., *Combust. Flame* 115:210 (1998).
20. Masri, A. R., and Pope, S. B., *Combust. Flame* 81:13 (1990).
21. Saxena, V., and Pope, S. B., in *Twenty-Seventh Symposium (International) on Combustion*, The Combustion Institute, Pittsburgh, 1998, p. 1081.
22. Saxena, V., and Pope, S. B., *Combust. Flame* 117:340 (1999).
23. Vervisch, L., in *Modeling of Combustion and Turbulence*, VKI 1992-03, von Karman Institute for Fluid Dynamics, 1992.
24. Dopazo, C., *Phys. Fluids A* 18:389 (1975).
25. Janicka, J., Kolbe, W., and Kollman, W., *J. Nonequilib. Thermodyn.* 4:47 (1979).
26. Yang, B., and Pope, S. B., *Combust. Flame* 112:16 (1998).
27. James, S., Anand, M. S., Razdan, M. K., and Pope, S. B., in *Proceedings of ASME Turbo. and Expo. Land, Sea and Air '99*, The 44th ASME Gas Turbine and AeroEngine Technical Congress, Indianapolis, IN, 1999.
28. *Fourth International Workshop on Measurement and Computation of Turbulent Nonpremixed Flames*, Darmstadt, Germany, 1999.
29. Pope, S. B., *Phys. Fluids* 6:973 (1994).
30. Xu, J., and Pope, S. B., in *Engineering Turbulence Modelling and Measurements* (W. Rodi and D. Laurence, Eds.), Vol. 4, Elsevier Science Publisher, Amsterdam, 1999, p. 795.
31. Wilcox, D. C., *Turbulence Modeling for CFD*, DCW Industries, Inc., La Cañada, CA, 1993.
32. Van Slooten, P. R., and Pope, S. B., *Flow Turb. Combust.* 62:295 (1999).
33. Xu, J., and Pope, S. B., *Combust. Flame* (to be submitted), 2000.
34. Norris, A. T., and Pope, S. B., *Combust. Flame* 83:27 (1991).
35. Masri, A. R., Subramaniam, S., and Pope, S. B., in *Twenty-Sixth Symposium (International) on Combustion*, The Combustion Institute, Pittsburgh, 1996, p. 49.
36. Chen, H.-D., Chen, S.-Y., and Kraichnan, R. H., *Phys. Rev. Lett.* 63:2657 (1989).
37. Spalding, D. B., *Chem. Eng. Sci.* 26:95 (1971).
38. Béguier, C., Dekeyser, I., and Launder, B. E., *Phys. Fluid* 21:307 (1978).
39. Panchapakesan, N. R., and Lumley, J. L., *J. Fluid Mech.* 246:225 (1993).
40. Subramaniam, S., and Pope, S. B., *Combust. Flame* 117:732 (1999).
41. Dreeben, T. D., and Pope, S. B. (1992). Technical Report FDA 92-13, Cornell University.
42. Pope, S. B. (1995). Technical Report FDA 95-06, Cornell University.
43. Pope, S. B., in *Turbulence and Molecular Processes in Combustion*, Elsevier Science Inc., New York, 1993.
44. Xu, J. (2000). Ph.D. thesis, Cornell University.
45. Xu, J., and Pope, S. B. (1999). Technical Report FDA 99-06, Cornell University.
46. Subramaniam, S. (1997). Ph.D. thesis, Cornell University.
47. Chen, J. Y., Personal communication.
48. Peters, N. (2000). *Turbulent Combustion*. Cambridge University Press, Cambridge, U.K.
49. Corrsin, S., *J. Fluid Mech.* 11:487 (1961).
50. Muradoglu, M., Pope, S. B., Jenny, P., and Caughey, D. A., *J. Comput. Phys.* 154:342 (1999).

Received 27 January 2000; revised 7 April 2000; accepted 26 April 2000